

FLOW MATCHING FOR ACCELERATED SIMULATION OF ATOMIC TRANSPORT IN MATERIALS

Juno Nam, Sulin Liu, Gavin Winter, KyuJung Jun, Soojung Yang, Rafael Gómez-Bombarelli
Massachusetts Institute of Technology

ABSTRACT

We introduce LIFLOW, a generative framework to accelerate molecular dynamics (MD) simulations for crystalline materials that formulates the task as conditional generation of atomic displacements. The model uses flow matching, with a *Propagator* submodel to generate atomic displacements and a *Corrector* to locally correct unphysical geometries, and incorporates an adaptive prior based on the Maxwell–Boltzmann distribution to account for chemical and thermal conditions. We benchmark LIFLOW on a dataset comprising 25-ps trajectories of lithium diffusion across 4,186 solid-state electrolyte (SSE) candidates at four temperatures. The model obtains a consistent Spearman rank correlation of 0.7–0.8 for lithium mean squared displacement (MSD) predictions on unseen compositions. Furthermore, LIFLOW generalizes from short training trajectories to larger supercells and longer simulations while maintaining high accuracy. With speed-ups of up to 600,000 \times compared to first-principles methods, LIFLOW enables scalable simulations at significantly larger length and time scales.

1 INTRODUCTION

Atomic transport is a fundamental process that governs the performance of materials in various technologies, including energy storage, catalysis, and electronic devices. Solid-state electrolytes (SSEs) are a prime example, emerging as a safer and more stable alternative to liquid electrolytes commonly used in lithium-ion batteries (Bachman et al., 2016). The study and design of SSEs rely on fast and accurate atomistic simulation techniques to model the intricate ionic diffusion behaviors that dictate the atomic transport in these materials. The standard method, *ab initio* molecular dynamics (AIMD), involves costly density functional theory (DFT) calculations for each propagation step in the scale of femtoseconds. Hence, their application is limited to small spatiotemporal scales and a few simulations, often insufficient for characterizing diffusive dynamics or screening candidate materials. Recently, universal machine learning interatomic potentials (MLIPs), trained on large-scale DFT calculations, have emerged as a promising alternative (Friederich et al., 2021; Ko & Ong, 2023). However, even with MLIPs, dynamics must be discretized in sufficiently small time steps to ensure stable and accurate propagation (Fu et al., 2023a) and are still too slow to enable scalable simulation of materials to perform high-throughput screening from large material databases.

To accelerate MD simulations for small bio/organic molecules, methods such as Timewarp (Klein et al., 2023a), Implicit Transfer Operator Learning (ITO, Schreiner et al. (2023)), Score Dynamics (SD, Hsu et al. (2024)), and Force-Guided Bridge Matching (FBM, Yu et al. (2024)) have been proposed. These methods leverage a generative model to propagate the conformational distribution from time τ to time $\tau + \Delta\tau$, where $\Delta\tau$ is much larger than the typical MD time steps. A similar approach has been applied to coarse-grained polymeric electrolyte simulations in Fu et al. (2023b).

In the context of all-atom simulations of crystalline materials across different temperatures, these methods do not account for symmetries or handle various atom types under various simulation conditions. This work aims to address this by developing a tailored, flow-matching-based, generative acceleration framework designed for scalable and cost-effective simulations of crystalline materials and diffusive dynamics in SSEs. The key objective is to construct a model capable of accurately reproducing relevant kinetic observables, such as mean squared displacement (MSD) and self-diffusivity of mobile ions, in comparison to long MD simulations using MLIPs or AIMD.

Our contributions are as follows:

- We introduce the task of generative acceleration of MD for crystalline materials, formulating it as the conditional generation of atomic displacements. Our approach accounts for periodic boundary conditions and generalizes effectively across different supercell sizes.
- We develop a flow matching approach with a physically motivated adaptive prior to account for chemical and thermal conditions, along with a corrector mechanism to ensure stability.
- Additionally, we contribute a trajectory dataset based on MLIPs, designed to benchmark performance across diverse material systems and temperature conditions.

2 BACKGROUND

2.1 PRELIMINARIES

Crystalline materials and representation The crystal structure, assuming perfect order with translational symmetry, can be idealized as an infinite repetition of atoms, each assigned an atom type from the periodic table \mathcal{A} , within a unit cell with periodic boundary conditions. In this work, the structure of a material with n atoms in the unit cell is represented by the tuple $\mathcal{M} = (\mathbf{X}, \mathbf{L}, \mathbf{a})$, where $\mathbf{X} = (\mathbf{x}_1, \mathbf{x}_2, \dots, \mathbf{x}_n)^\top \in \mathbb{R}^{n \times 3}$ denotes the Cartesian coordinates of the atoms, $\mathbf{L} = (\mathbf{l}_1, \mathbf{l}_2, \mathbf{l}_3)^\top \in \mathbb{R}^{3 \times 3}$ is the lattice matrix, and $\mathbf{a} \in \mathcal{A}^n$ is the atom types. We impose a graph structure on the material by connecting pairs of nearby atoms with edges (Schütt et al., 2017), possibly across unit cell boundaries. An edge $((i, j), \mathbf{k}) \in \llbracket 1, n \rrbracket^2 \times \mathbb{Z}^3$ is formed between atoms i and j if the distance between atom i and atom j , displaced by \mathbf{k} unit cells from i , is smaller than the cutoff, i.e., $\|\mathbf{x}_j + \mathbf{k}\mathbf{L} - \mathbf{x}_i\|_2 < r_{\text{cutoff}}$. An $a \times b \times c$ supercell of \mathcal{M} is defined as

$$(\mathbf{X}', \mathbf{L}', \mathbf{a}') = (\oplus_{\kappa=1}^{abc} (\mathbf{X} + \mathbf{1}_n \otimes \mathbf{k}_\kappa), \mathbf{L} \text{diag}(a, b, c), \oplus_{\kappa=1}^{abc} \mathbf{a}), \quad (1)$$

where \oplus denotes concatenation, \otimes is the outer product, and $\mathbf{k}_\kappa \in \mathbb{Z}_a \times \mathbb{Z}_b \times \mathbb{Z}_c$ represents the index of unit cell repetitions. Although the method is designed for general crystalline materials, the primary application of this work is on lithium SSEs, which are further discussed in Appendix A.1.

Molecular dynamics for materials MD is a simulation methodology used to sample ensembles of configurations or trajectories of atomistic systems by solving the equation of motion, $M\ddot{\mathbf{X}}_\tau = -\nabla U(\mathbf{X}_\tau)$, over time τ ,¹ where $M = \text{diag}(\mathbf{m})$ is the diagonal matrix of atomic masses, $\mathbf{m} = \mathbf{m}(\mathbf{a})$, and $U(\mathbf{X})$ is the potential energy (Frenkel & Smit, 2023). Given the initial position \mathbf{X}_0 and the velocity $\dot{\mathbf{X}}_0$, typically sampled from the Maxwell–Boltzmann distribution, the equation of motion is usually discretized and propagated with a time step of 0.5–2 fs, depending on the fastest motion of the system. For organic and biomolecules with a limited number of atom types, classical force fields with specified functional forms are routinely used to approximate the system energy with reasonable accuracy. However, for inorganic solid systems containing various elements across the periodic table, the parametrization of classical force fields is challenging, and $U(\cdot)$ is often derived from quantum mechanical calculations (*ab initio* MD), which are computationally much more expensive and scale poorly ($\mathcal{O}(n^3)$ in theory). For more details, refer to Appendix A.2.

Machine learning interatomic potentials Due to the high computational cost of *ab initio* calculations, machine learning interatomic potentials (MLIPs) based on graph neural networks have been developed to approximate the results of the quantum calculations (Friederich et al., 2021; Ko & Ong, 2023). Recent advances in universal MLIPs, such as MACE-MP-0 (Batatia et al., 2024) and CHGNet (Deng et al., 2023), enable faster simulations and linear scaling with respect to number of atoms, but pre-trained models often tend to overestimate the kinetic properties (Deng et al., 2024). We employed MLIPs to generate our trajectory dataset of lithium-containing materials to demonstrate chemical transferability across different materials.

Flow matching Flow matching (Lipman et al., 2023) is a generative modeling framework in which samples from the prior distribution $x_0 \sim p_0(x)$ are transported to samples from the data distribution $x_1 \sim q(x)$ by a time-dependent vector field $u_t(x)$ ($t \in [0, 1]$). The vector field generates a flow ψ_t defined with $\psi_0(x) = x$ and $(d/dt)\psi_t(x) = u_t(\psi_t(x))$ and a probability path $p_t(x) = [\psi_t]_* p_0(x)$.

¹In this work, we denote physical time by τ and flow matching time by t . For clarity, we omit the physical time when it does not cause ambiguity, e.g., \mathbf{D}_0 and \mathbf{D}_1 correspond to $t = 0$ and 1, respectively.

The data conditional vector field $u_t(x|x_1)$ is available in closed form for the commonly used Gaussian probability path, i.e., $p_t(x|x_1) = \mathcal{N}(x; \mu_t(x_1), \sigma_t(x_1)^2 \mathbf{I})$. The marginal vector field model $v_t(x; \theta)$ is parametrized by a neural network and learned by the following regression objective:

$$\mathcal{L}_{\text{CFM}}(\theta) = \mathbb{E}_{t \sim \mathcal{U}(t; 0, 1), x_1 \sim p_1(x), x \sim p_t(x|x_1)} \|v_t(x; \theta) - u_t(x|x_1)\|^2. \quad (2)$$

2.2 RELATED WORKS

ML surrogates for dynamics simulation Several works have explored ML surrogates for time-coarsened dynamics by learning transition probability densities. Timewarp (Klein et al., 2023a) employs a conditional normalizing flow (CNF) with Markov chain Monte Carlo sampling, while ITO (Schreiner et al., 2023) is a conditional diffusion model designed as an arbitrary time-lag propagator. SD (Hsu et al., 2024) learns the score function of the transition density, and FBM (Yu et al., 2024) uses a conditional bridge process with a correction mechanism based on intermediate force fields. These methods are applied to biomolecular simulations, with less chemical diversity and different symmetry requirements and task formulations from our work. Notably, Fu et al. (2023b) targets non-Markovian dynamics in coarse-grained polymeric materials by learning the acceleration and using a score-based corrector. While coarse-graining allows for the explicit modeling of dynamics over longer timesteps using the equations of motion, our task requires all-atom modeling, necessitating a generative surrogate for the dynamics. Moreover, none of these approaches explored a task-specific prior with flow matching, which was crucial to the improved performance in this work.

Generative models for materials As a time-hopping conditional generative model for material structures, our approach shares design principles with crystal generation models (Xie et al., 2022; Jiao et al., 2023; AI4Science et al., 2023; Zeni et al., 2024; Yang et al., 2024; Miller et al., 2024), which use diffusion or flow matching to generate atomic identities and positions within a unit cell. While these methods often handle position generation as fractional coordinates with periodic boundaries, our task requires modeling displacements in Cartesian coordinates directly without wrapping positions back into the unit cell (Appendix A.3).

Prior design While the normal distribution $\mathcal{N}(\mathbf{0}, \mathbf{I})$ is commonly used in diffusion and flow-based generative models, incorporating task-specific inductive biases into the prior distribution can improve generative performance. Lee et al. (2022) introduced data-dependent priors in diffusion models, Guan et al. (2023) used decomposed priors for ligand generation, Jing et al. (2023) applied harmonic priors for protein structure generation, and Irwin et al. (2024) employed scale-based priors for molecular conformation. The common goal in these methods is to reduce the transport cost by initializing the prior closer to the data distribution. We use a physically motivated prior based on the Maxwell–Boltzmann distribution for this, which additionally accounts for differences between atom types and reflects thermal and phase conditions.

3 METHODS

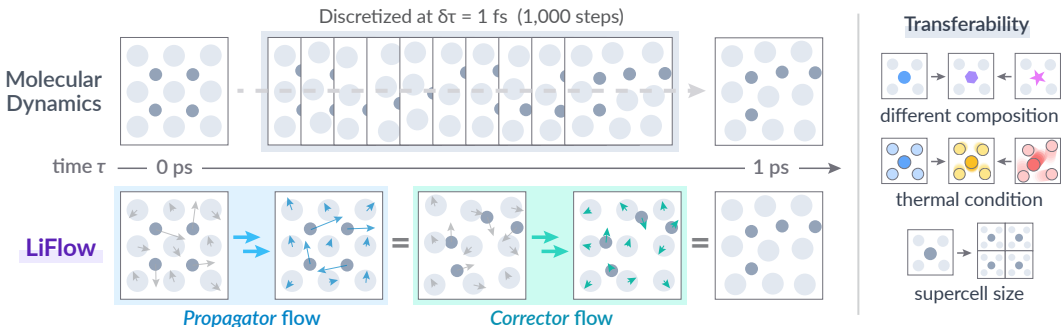


Figure 1: **LiFlow scheme.** LiFlow is a generative acceleration framework for MD simulations for crystalline materials, with *Propagator* and *Corrector* components leveraging a conditional flow matching scheme for accurate generation of atomic displacements during time propagation.

The LiFLOW framework is illustrated in Fig. 1. We begin by outlining the problem of generating atomic displacements to accelerate simulations and discussing the symmetry constraints necessary for scalable generation. Next, we propose a physically motivated prior and a flow model parametrization that adheres to these constraints, followed by the training and inference processes.

3.1 PROBLEM SETTING

Similar to the ML-based MD acceleration methods in Section 2.2, our goal is to model the transition probability density of a material structure over a time interval $\Delta\tau$, conditioned on the temperature T : $p(\mathcal{M}_{\tau+\Delta\tau}|\mathcal{M}_\tau, T)$. For this task, we fix the lattice \mathbf{L} (constant volume) and atom types \mathbf{a} , and set $\Delta\tau$ as 1 ps, which is 1,000 times larger than the usual MD time step of 1 fs. In MD simulations used to model the kinetics of materials, *unwrapped* coordinates are utilized, meaning atomic coordinates are not confined to the unit cell, in order to keep track of the atomic displacements. As a result, unlike previous works on MD for biomolecules with one connected component with the fixed center of mass, the distribution of positions does not have a finite support. Therefore, we opt to model the distribution of *displacements* over time interval $\Delta\tau$, $\mathbf{D}_{\Delta\tau} := \mathbf{X}_{\tau+\Delta\tau} - \mathbf{X}_\tau$. In summary,

Task: learn the conditional distribution of atomic displacements $p(\mathbf{D}_{\Delta\tau}|\mathbf{X}_\tau, \mathbf{L}, \mathbf{a}, T)$ from a dataset of time-separated pairs of structures $\mathcal{D} = \{((\mathbf{X}_\tau, \mathbf{X}_{\tau+\Delta\tau}), \mathbf{L}, \mathbf{a}, T)\}$, extracted from MD trajectories across various material compositions and temperatures.

More details and rationale on the task design choices can be found in Appendix A.3.

3.2 CONDITIONAL FLOW MATCHING FOR TIME PROPAGATION

3.2.1 SYMMETRY CONSIDERATIONS

The conditional probability density of displacements is invariant to permutation of atomic indices, global translation and lattice shift of atomic coordinates, global rotation applied to relevant variables, and supercell choice (we omit the physical time τ and $\Delta\tau$ here for brevity):

$$p(\mathbf{D}|\mathbf{X}, \mathbf{L}, \mathbf{a}, T) = p(\mathbf{P}\mathbf{D}|\mathbf{P}\mathbf{X}, \mathbf{L}, \mathbf{P}\mathbf{a}, T), \quad \mathbf{P} \in S_n \text{ (permutation)} \quad (3)$$

$$p(\mathbf{D}|\mathbf{X}, \mathbf{L}, \mathbf{a}, T) = p(\mathbf{D}|\mathbf{X} + \mathbf{1}_n \otimes \mathbf{t}, \mathbf{L}, \mathbf{a}, T), \quad \mathbf{t} \in \mathbb{R}^3 \text{ (global translation)} \quad (4)$$

$$p(\mathbf{D}|\mathbf{X}, \mathbf{L}, \mathbf{a}, T) = p(\mathbf{D}|\mathbf{X} + \mathbf{Z}\mathbf{L}, \mathbf{L}, \mathbf{a}, T), \quad \mathbf{Z} \in \mathbb{Z}^{n \times 3} \text{ (lattice periodicity)} \quad (5)$$

$$p(\mathbf{D}|\mathbf{X}, \mathbf{L}, \mathbf{a}, T) = p(\mathbf{D}\mathbf{R}|\mathbf{X}\mathbf{R}, \mathbf{L}\mathbf{R}, \mathbf{a}, T), \quad \mathbf{R} \in \text{O}(3) \text{ (rotation/reflection)} \quad (6)$$

$$p(\mathbf{D}|\mathbf{X}, \mathbf{L}, \mathbf{a}, T) = p(\mathbf{D}'|\mathbf{X}', \mathbf{L}', \mathbf{a}', T), \quad \text{(supercell, defined as Eq. (1))} \quad (7)$$

In general, to model the invariant densities with CNFs, we need an invariant base distribution and equivariant flow vector fields (Köhler et al., 2020; Klein et al., 2023b). Translational invariances Eqs. (4) and (5) and supercell invariance Eq. (7) are satisfied by our choice of representation for materials (Section 2.1). For O(3) and S_n symmetries, we model our prior and flow according to the following proposition.

Proposition 1 *Given an invariant base distribution $p_0(\mathbf{D}_0)$ satisfying Eqs. (3) and (6) and an equivariant conditional vector field $u_t(\mathbf{D}_t|\mathbf{D}_1)$ with the following properties:*

$$u_t(\mathbf{P}\mathbf{D}_t|\mathbf{P}\mathbf{D}_1, \mathbf{P}\mathbf{X}, \mathbf{L}, \mathbf{P}\mathbf{a}, T) = \mathbf{P}u_t(\mathbf{D}_t|\mathbf{D}_1, \mathbf{X}, \mathbf{L}, \mathbf{a}, T), \quad \mathbf{P} \in S_n \quad (8)$$

$$u_t(\mathbf{D}_t\mathbf{R}|\mathbf{D}_1\mathbf{R}, \mathbf{X}\mathbf{R}, \mathbf{L}\mathbf{R}, \mathbf{a}, T) = u_t(\mathbf{D}_t|\mathbf{D}_1, \mathbf{X}, \mathbf{L}, \mathbf{a}, T)\mathbf{R}, \quad \mathbf{R} \in \text{O}(3) \quad (9)$$

the generated conditional probability path $p_{t|1}(\mathbf{D}_t|\mathbf{D}_1)$ is invariant. Furthermore, given that the data distribution $q(\mathbf{D}_1)$ is invariant, the marginal probability path $p_t(\mathbf{D}_t)$ is also invariant.

Note that the group actions of S_n and O(3) on the optional conditional variable \mathbf{D}_1 are the same as their actions on \mathbf{D}_t . The proof is given in Appendix B.

3.2.2 CHOICE OF PRIOR

We consider a Gaussian prior, $\mathbf{D}_0 \sim \mathcal{N}(\mathbf{D}_0; \mathbf{0}, \Sigma \otimes \mathbf{I}_3)$, with a diagonal covariance $\Sigma = \text{diag}(\boldsymbol{\sigma})^2$, where $\boldsymbol{\sigma} = \boldsymbol{\sigma}(\mathbf{a}, T) \in \mathbb{R}^n$ is equivariant to atom index permutation. This prior distribution satisfies

the symmetry constraints Eqs. (3) to (7). In MD simulation of materials, atomic displacements tend to be larger for lighter atoms and at higher temperatures. In the short-time, non-interacting limit, the displacements can be expressed as $\mathbf{D}_{\delta\tau} = \dot{\mathbf{X}}_{\tau}\delta\tau$, where the marginal distribution of velocity follows the Maxwell–Boltzmann distribution, $\dot{\mathbf{X}}_{\tau} \sim \mathcal{N}(\dot{\mathbf{X}}_{\tau}; \mathbf{0}, \text{diag}(k_{\text{B}}T/\mathbf{m}) \otimes \mathbf{I}_3)$, with k_{B} being the Boltzmann constant. Thus, it is reasonable to initialize the noise from a *scaled* Maxwell–Boltzmann distribution with $\sigma = \sigma \cdot (k_{\text{B}}T/\mathbf{m})^{1/2}$, where σ is a constant hyperparameter controlling the scale.

In the specific context of AIMD simulations in this work, where the simulations are often conducted at elevated temperatures, the material may undergo phase transitions (e.g., from solid to liquid) within the temperature range covered by the dataset. Additionally, for lithium-based solid-state electrolytes, lithium atoms may exhibit displacements several orders of magnitude larger than those of non-lithium (frame) atoms. To account for these variations, we introduce a material-dependent *adaptive* scaling factor for the Maxwell–Boltzmann distribution:

$$\sigma = [\sigma_{\text{Li}}(\mathcal{M}_0, T) \cdot \mathbb{I}_{\mathbf{a}=\text{Li}} + \sigma_{\text{frame}}(\mathcal{M}_0, T) \cdot \mathbb{I}_{\mathbf{a}\neq\text{Li}}] \odot (k_{\text{B}}T/\mathbf{m})^{1/2}, \quad (10)$$

where $\sigma_{\mathcal{S}}$ selects a scale value, either $\sigma_{\mathcal{S}}^{\text{small}}$ or $\sigma_{\mathcal{S}}^{\text{large}}$ (both hyperparameters), based on the output of a binary classifier that predicts whether the displacements for species \mathcal{S} (lithium or frame) will be small or large. The classifier utilizes temperature and the average-pooled atomic invariant features of \mathcal{S} , extracted from a pre-trained MACE model, based on the initial material structure \mathcal{M}_0 . Further details about the classifier model are provided in Appendix D.1.

3.2.3 FLOW PARAMETRIZATION

Conditional flow matching Following Pooladian et al. (2023), we select the linear interpolation between the prior sample and the data sample as a conditional flow:

$$u_t(\mathbf{D}_t|\mathbf{D}_1) = \frac{\mathbf{D}_1 - \mathbf{D}_t}{1 - t} \quad \text{and} \quad \mathbf{D}_t = \psi_t(\mathbf{D}_0|\mathbf{D}_1) = (1 - t)\mathbf{D}_0 + t\mathbf{D}_1. \quad (11)$$

This satisfies the symmetry constraints in Eqs. (8) and (9). The marginal flow approximator $v_t(\mathbf{D}_t, \mathbf{X}_{\tau}, \mathbf{L}, \mathbf{a}, T; \theta)$ should also respect these symmetry constraints. We adopt the PAINN model (Schütt et al., 2021) to balance expressiveness with inference speed. PAINN is an equivariant graph neural network that outputs scalar and vector quantities based on the atomistic graph structure, incorporating scalar and vector node features. The structure is encoded using a radial basis function expansion of atomic distances and the unit vector directions along edges. We observed that encoding the intermediate structure $\mathbf{X}_{\tau} + \mathbf{D}_t$ significantly improves prediction performance (Table A1). Thus, we modify the message-passing layers of PAINN to accept two structural inputs: \mathbf{X}_{τ} and $\mathbf{X}_{\tau} + \mathbf{D}_t$. Additionally, the intermediate displacements \mathbf{D}_t are used to construct the vector node features. Further details on the model architecture and modifications are given in Appendix D.2.

Propagator and Corrector models

While, in theory, a single generative model should suffice to learn the density, prediction errors would arise from two sources: inaccuracies in the marginal flow prediction and discretization errors in the flow integration. Moreover, since the trajectory generation is performed autoregressively, applying the generative model iteratively compounds these errors over time. To address this, in addition to the flow matching model described earlier (“*Propagator*”), we introduce an auxiliary flow matching model named *Corrector*, inspired by Fu et al. (2023b), to rectify potential errors in the predicted displacements.

Although the *Corrector* model is intended to correct errors in the final displacement resulting from the integration of *Propagator*, di-

Algorithm 1: LIFLOW Inference

Input: Initial position \mathbf{X}_0 , lattice \mathbf{L} , atom types \mathbf{a} , atomic masses $\mathbf{m}(\mathbf{a})$, temperature T

Output: Predicted position \mathbf{X}_{τ} at $\tau = N_{\text{step}}\Delta\tau$

Determine the prior from \mathbf{X}_0 , \mathbf{L} , \mathbf{a} , \mathbf{m} , and T

for $i_{\tau} \leftarrow 0$ **to** $N_{\text{step}} - 1$ **do**

$\tau \leftarrow i_{\tau}\Delta\tau$ and $\tau' \leftarrow (i_{\tau} + 1)\Delta\tau$

Sample \mathbf{D} from the *Propagator* prior

for $i \leftarrow 0$ **to** $N_{\text{flow}} - 1$ **do**

$\mathbf{D} \leftarrow \mathbf{D} + \text{Propagator}(\mathbf{D}, \mathbf{X}_{\tau}, \mathbf{L}, \mathbf{a}, T, t)/N_{\text{flow}}$

$\tilde{\mathbf{X}}_{\tau'} \leftarrow \mathbf{X}_{\tau} + \mathbf{D}$ // Propagated \mathbf{x}

Sample \mathbf{D} from the *Corrector* prior

for $i \leftarrow 0$ **to** $N_{\text{flow}} - 1$ **do**

$\mathbf{D} \leftarrow \mathbf{D} + \text{Corrector}(\mathbf{D}, \tilde{\mathbf{X}}_{\tau'}, \mathbf{L}, \mathbf{a}, T, t)/N_{\text{flow}}$

$\mathbf{X}_{\tau'} \leftarrow \tilde{\mathbf{X}}_{\tau'} + \mathbf{D}$ // Corrected \mathbf{x}

$\mathbf{X}_{\tau'} \leftarrow \mathbf{X}_{\tau'} - \text{CoM}(\mathbf{X}_{\tau'}, \mathbf{m}) + \text{CoM}(\mathbf{X}_{\tau}, \mathbf{m})$

rectly mapping the generated output to an actual data sample to compute the target correction value can be complex, as it may require differentiating through the flow integration. Therefore, we decouple the *Propagator* and *Corrector* models, training the *Corrector* to denoise positional noise of arbitrary small scale. Given a perturbed configuration $\tilde{\mathbf{X}}_\tau = \mathbf{X}_\tau + \mathbf{D}$, where the noise displacement is sampled from $\mathbf{D}|\boldsymbol{\sigma}' \sim \mathcal{N}(\mathbf{D}; \mathbf{0}, \text{diag}(\boldsymbol{\sigma}')^2 \otimes \mathbf{I}_3)$ with the noise scale $\boldsymbol{\sigma}' \sim \mathcal{U}(\boldsymbol{\sigma}'; \mathbf{0}, \sigma_{\max} \mathbf{1}_n)$, the flow is trained to generate the possible denoising displacements $-\mathbf{D}$ conditioned on $\tilde{\mathbf{X}}_\tau$.

3.2.4 TRAINING AND INFERENCE

LIFLOW training We train the model using time-separated pairs of structures, $((\mathbf{X}_\tau, \mathbf{X}_{\tau+\Delta\tau}), \mathbf{L}, \mathbf{a}, T)$, sampled from MD trajectories in the training set. First, the prior displacements are sampled based on the possible choices outlined in Section 3.2.2. The *Propagator* and *Corrector* are trained to approximate the marginal flows toward the distributions of the possible propagating displacements, $\mathbf{X}_{\tau+\Delta\tau} - \mathbf{X}_\tau$, and denoising displacements, $\mathbf{X}_{\tau+\Delta\tau} - \tilde{\mathbf{X}}_{\tau+\Delta\tau}$, respectively. These are conditioned on the previous structure, \mathbf{X}_τ , and the noisy structure, $\tilde{\mathbf{X}}_{\tau+\Delta\tau}$, respectively. Given interpolated displacements \mathbf{D}_t and the corresponding conditional variables, both models are trained to match the ground truth conditional flow $u_t(\mathbf{D}_t|\mathbf{D}_1)$ using the regression loss Eq. (2). Detailed training algorithms are reported in Appendix D.3.

LIFLOW inference The inference procedure is provided in Algorithm 1. Starting from the initial atom positions \mathbf{X}_0 , we alternate between *Propagator* and *Corrector* flow integration for N_{step} steps, generating the trajectory $\{\mathbf{X}_{i\Delta\tau}\}_{i=0}^{N_{\text{step}}}$ with a total duration of $\tau = N_{\text{step}}\Delta\tau$. The flow integration for both the *Propagator* and *Corrector* begins by sampling prior displacements \mathbf{D}_0 from the chosen prior distribution. These displacements are then updated over N_{flow} steps using Euler’s method, based on the predicted marginal flow. Since MD simulations are often performed with a fixed center-of-mass (CoM) position, defined as $\text{CoM}(\mathbf{X}, \mathbf{m}) = \sum_j m_j \mathbf{x}_j / \sum_j m_j$, we correct for any CoM drift after each *Propagator–Corrector* inference step.

4 EXPERIMENTS

4.1 DATASETS AND METRICS

Universal MLIP dataset To train a compositionally transferable generative model for time-shifting conformational distributions, long-time simulation trajectories that span a diverse range of compositional spaces in solid-state materials are required. A total of 4,186 stable lithium-containing structures were retrieved from the Materials Project database (Jain et al., 2013) to capture various modes of lithium-ion dynamics across different compositions. For each structure, 25 ps MD simulations were performed using the MACE-MP-0 small universal MLIP model (Batatia et al., 2024) at temperatures of 600, 800, 1000, and 1200 K, with a time step of 1 fs (25k steps per structure). The distribution of elements in these structures, shown in Fig. A1a, spans 77 elements across the periodic table. The mean squared displacement (MSD) of lithium atoms for each structure over the 25 ps trajectories is shown in Fig. A1b, indicating that the dataset captures a broad range of atomic environments and dynamic behaviors. The dataset is divided into training (90%) and test (10%) sets based on material composition, with the validation set sampled from the training portion. Details of the simulations and dataset statistics are provided in Appendix C.1.

AIMD datasets To evaluate the ability to extend accurate atomistic dynamics from short AIMD simulations, we employed two sets of AIMD trajectories that exhibit diffusive lithium dynamics. The first set includes LPS (Li_3PS_4) simulations from Jun et al. (2024b), with ~ 250 ps trajectories for 128-atom structures of α -, β -, and γ -LPS, conducted at 600–800 K. The second set comprises LGPS ($\text{Li}_{10}\text{GeP}_2\text{S}_{12}$) simulations from López et al. (2024), which includes ~ 150 ps MD trajectories for a $2 \times 2 \times 1$ supercell (200 atoms) of LGPS at temperatures of 650, 900, 1150, and 1400 K. We used the first 25 ps of each trajectory as the training set. Refer to Appendix C.2 for the rationale behind system selection and further details.

Metrics To quantify the prediction of kinetic observables, we compared the MSD of lithium and frame atoms between generated and reference trajectories. The MSD for a set of atoms \mathcal{S} is defined as Eq. (12):

$$\text{MSD}_{\mathcal{S}}(\tau) = \frac{1}{|\mathcal{S}|} \sum_{i \in \mathcal{S}} \|\mathbf{x}_{\tau,i} - \mathbf{x}_{0,i}\|^2 \quad (12) \quad D_{\mathcal{S}}^* = \lim_{\tau \rightarrow \infty} \frac{\text{MSD}_{\mathcal{S}}(\tau)}{6\tau} \quad (13)$$

Given the wide range of magnitudes in the raw MSD values, we compared the log MSD values (with base 10, MSD in units of \AA^2) to the reference trajectories. We report the mean absolute error (MAE) and Spearman’s rank correlation (ρ) for the log MSD predictions on the universal MLIP dataset.

In the long-time limit, the MSD grows linearly with time, with a rate proportional to the self-diffusivity $D_{\mathcal{S}}^*$ (Eq. (13)). This is calculated using Bayesian regression of MSD against time (McCluskey et al., 2024a,b). According to the Arrhenius relationship, the temperature dependence of diffusivity follows $\log D^*(T) = \log D_0^* - E_A/k_B T$, where E_A is the activation energy. Since activation energy is a key measure of the barrier to lithium diffusion in materials science literature, we also verify whether E_A is accurately reproduced in the LGPS AIMD dataset.

To evaluate the reproduction of structural features, we compare the all-particle radial distribution function (RDF), $g(r)$, defined as:

$$g(r) = \frac{1}{4\pi r^2} \frac{1}{\rho n} \sum_i \sum_{j \neq i} \delta(r - \|\mathbf{x}_i - \mathbf{x}_j\|), \quad (14)$$

where ρ is the number density of atoms. This is averaged over the latter parts of the simulation, after discarding a short induction period (5 ps). The accuracy is quantified by the RDF MAE = $(1/r_{\text{cut}}) \int_0^{r_{\text{cut}}} |\hat{g}(r) - g(r)| dr$, with $r_{\text{cut}} = 5 \text{\AA}$.

4.2 UNIVERSAL MODEL

Inference setup We conducted LIFLOW inference iteratively for $N_{\text{step}} = 25$ steps to simulate dynamics over 25 ps with a time step of $\Delta\tau = 1$ ps. Each inference step involves $N_{\text{flow}} = 10$ flow matching iterations of both *Propagator* and *Corrector* models. During each inference process for a given structure, we terminated when either the maximum number of steps (N_{step}) was reached or the model prediction diverged due to instabilities.

Table 1: **Effect of prior design.** Evaluation metrics for the *Propagator* model across different priors: isotropic, uniform scale Maxwell–Boltzmann (uniform M–B), and adaptive scale M–B ([†]*regression*: non-generative, directly predicting displacements). Standard deviations are from three independent generations.

Train T (K)	Inference T (K)	Prior	log MSD _{Li} MAE (↓)	log MSD _{Li} ρ (↑)	log MSD _{frame} MAE (↓)	Stable traj. % (↑)
800	800	<i>Regression</i> [†]	1.636	0.535	0.876	90.2
		Isotropic	0.498±0.003	0.753±0.008	0.318±0.008	98.6±0.2
		Uniform M–B	0.396 ±0.006	0.779 ±0.009	0.274 ±0.003	99.4 ±0.1
All	600	Uniform M–B	0.345 ±0.003	0.740 ±0.009	0.257 ±0.006	99.8 ±0.2
		Adaptive M–B	0.376±0.005	0.709±0.003	0.286±0.001	99.6±0.2
	800	Uniform M–B	0.417±0.007	0.737±0.011	0.307±0.003	99.8 ±0.2
		Adaptive M–B	0.385 ±0.004	0.759 ±0.008	0.294 ±0.001	99.5±0.0
	1000	Uniform M–B	0.505±0.011	0.705±0.008	0.400±0.007	98.6 ±0.2
		Adaptive M–B	0.456 ±0.024	0.746 ±0.008	0.374 ±0.003	98.6 ±0.6
1200	Uniform M–B	0.448±0.006	0.788±0.003	0.493±0.003	95.5±0.5	
	Adaptive M–B	0.410 ±0.002	0.809 ±0.003	0.416 ±0.003	98.1 ±0.6	

Effect of the prior choice First, we compare the isotropic prior, with $\sigma = \sigma \cdot \mathbf{1}_n$, to the scaled Maxwell–Boltzmann prior, with $\sigma = \sigma \cdot (k_B T/m)^{1/2}$, to evaluate the impact of atom-type-specific scaling on the prior. To focus solely on the relative scale between atoms, we vary the scaling factor σ

for both the isotropic and Maxwell–Boltzmann priors at a fixed temperature (800 K), then compare the relevant metrics for the optimal σ in each case. The best results for isotropic ($\sigma = 10^{-1.5}$) and Maxwell–Boltzmann ($\sigma = 1$) priors are shown in the first row of Table 1, and the results across all scales are provided in Table A3. The scaled Maxwell–Boltzmann prior outperforms the isotropic prior in reproducing all kinetic metrics (log MSD), confirming that the relative scaling of priors among elements is crucial for performance across a wide range of compositions.

Next, we apply the scale determined in this experiment to the training and inference on trajectories across all temperatures, and compare to the adaptive scale Maxwell–Boltzmann prior (Eq. (10)). For the adaptive prior, we set the scale hyperparameters as $(\sigma_{\text{Li}}^{\text{low}}, \sigma_{\text{Li}}^{\text{high}}, \sigma_{\text{frame}}^{\text{low}}, \sigma_{\text{frame}}^{\text{high}}) = (1, 10, 10^{-0.5}, 10^{0.5})$, based on the observation that lithium atoms are generally more diffusive than the frame atoms. The metrics on trajectories for test set materials at each temperature are presented in Table 1. With the exception of the lowest temperature (600 K), where the prior classifier is mostly ineffective (see Fig. A2), the model using the adaptive prior outperforms the one with the uniform scale Maxwell–Boltzmann prior. This suggests that the mixture-of-priors approach effectively guides the flow model in capturing the scale of atomic movements. Additionally, note that the poor performance of direct regression-based displacement prediction (see Table 1, first row) highlights the necessity of generative modeling.

Table 2: **Effect of Corrector.** Both the *Predictor* (P) and *Corrector* (C) models were trained on the full set of temperature trajectories, and the adaptive scaling prior scheme was used.

Inference T (K)	Model	log MSD _{Li} MAE (\downarrow)	log MSD _{Li} ρ (\uparrow)	log MSD _{frame} MAE (\downarrow)	RDF MAE (\downarrow)	Stable traj. % (\uparrow)
600	P	0.376 \pm 0.005	0.709 \pm 0.003	0.286 \pm 0.001	0.118 \pm 0.0002	99.6 \pm 0.2
	$P + C$	0.348 \pm 0.004	0.744 \pm 0.012	0.241 \pm 0.002	0.069 \pm 0.0001	100.0 \pm 0.0
800	P	0.385 \pm 0.004	0.759 \pm 0.008	0.294 \pm 0.001	0.110 \pm 0.0004	99.5 \pm 0.0
	$P + C$	0.366 \pm 0.005	0.781 \pm 0.005	0.255 \pm 0.004	0.066 \pm 0.0000	100.0 \pm 0.0
1000	P	0.456 \pm 0.024	0.746 \pm 0.008	0.374 \pm 0.003	0.126 \pm 0.0004	98.6 \pm 0.6
	$P + C$	0.429 \pm 0.003	0.769 \pm 0.006	0.332 \pm 0.002	0.071 \pm 0.0001	99.8 \pm 0.1
1200	P	0.410 \pm 0.002	0.809 \pm 0.003	0.416 \pm 0.003	0.137 \pm 0.0004	98.1 \pm 0.6
	$P + C$	0.389 \pm 0.005	0.821 \pm 0.004	0.363 \pm 0.003	0.079 \pm 0.0002	99.6 \pm 0.1

Effect of the Corrector model In addition to the *Propagator* model with an adaptive scale prior, as determined in the previous experiment, we trained a *Corrector* model using a maximum noise scale of $\sigma_{\text{max}} = 0.25$ and a small uniform-scale Maxwell–Boltzmann prior with $\sigma = 0.1$. We then compared the kinetic metrics and the RDF MAE between the trajectories generated using only the *Propagator* and the combined *Propagator + Corrector* LiFLOW models, as shown in Table 2. We observed improved reproduction of static structural features, indicated by lower RDF MAE, across all temperatures when using the *Corrector* model. Notably, all kinetic metrics also showed improvement with the use of *Corrector*. Since the *Propagator* is a generative model of displacements conditioned on the current time step structure \mathbf{X}_τ , correcting errors in the conditional structure improves the accuracy of the predicted cumulative displacements, as reflected in the MSD metric.

Case studies The parity plot between log MSD values of reference and LiFLOW-generated trajectories at 800 K, along with visualized example trajectories, is shown in Fig. A4. We observed that the diffusive behavior in well-known solid-state electrolytes, such as Li₆PS₅Br (argyrodite, Fig. A4I), is accurately reproduced. It is important to note that the stability reported in Tables 1 and 2 refers to numerical stability—unlike the physical stability of MD trajectories, it is possible to generate numerically stable but physically fictitious dynamics, as illustrated in Fig. A4II.

4.3 AIMD MODELS

Training and inference Since we are training on the same composition, the *Propagator* error is expected to be smaller than that for the universal dataset, and we accordingly use a smaller maximum noise scale for the *Corrector*. For each dataset (LPS and LGPS), a single *Propagator* and *Corrector*

model is trained on the first 25 ps of trajectories across temperatures (and polymorph structures for LPS). Additional training and inference settings are provided in Appendix D.4.

Reproducing kinetic properties Fig. 2 shows the reference diffusivity values for LPS from the AIMD simulations (25 ps for training and ~ 250 ps full dataset) alongside the 250 ps LiFLOW inference results. Overall, the LiFLOW results match the order of magnitude of the reference simulations, successfully reproducing the diffusivity differences among the LPS polymorphs. This suggests that the model can detect subtle local structural variations between polymorphs and generate displacements accordingly. In cases where diffusive behavior is expected but not sufficiently captured in a 25 ps trajectory to yield robust diffusivity statistics, LiFLOW can “infill” the correct diffusive dynamics based on other simulations (Fig. 2a). However, when lithium hopping events become exceedingly rare, as in the case of γ -LPS at lower temperatures, the generative model suffers from mode collapse towards non-diffusive displacements, resulting in an underestimation of D^* (Fig. 2b).

Fig. 3 similarly presents the diffusivity values for LGPS from AIMD simulations and LiFLOW inference. For the $2 \times 2 \times 1$ supercell (Fig. 3, left), the temperature dependence of D^* , characterized by an activation energy of $E_A = 0.185$ eV, is consistent with the reference AIMD value (0.192 eV, Table 3). Although the 25 ps AIMD E_A (0.173 eV) lies outside the 95% CI of the longer AIMD, LiFLOW successfully matches the longer AIMD result and produces more reliable statistics with lower variance, owing to its extended simulation rollouts.

Reproducing structural features The diffusion trace in Fig. A5 shows that the generated dynamics and the reference dynamics explore different but symmetrically related sites in unwrapped coordinates. This confirms that the model is not merely memorizing the reference dynamics but is generalizing to physically equivalent configurations. Additionally, 2-D log probability densities² of lithium atoms are plotted along the x - y and y - z planes in Fig. A6. The log densities are accurately reproduced at lower temperatures, but deviate at higher temperatures, becoming noisier for LiFLOW, which results in a smoothing of the (free) energy landscape. As the displacements due to diffusion become larger and more varied at higher temperatures, we expect it to be more challenging to achieve high accuracy for static structural features under these conditions.

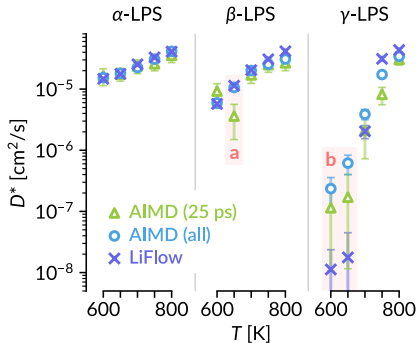


Figure 2: **Diffusivity for LPS.** Lithium D^* for polymorphs of LPS (Li_3PS_4). Values are derived from AIMD (25 ps training and ~ 250 ps full trajectories) and 250 ps LiFLOW inference.

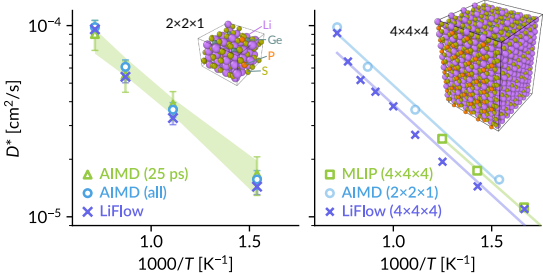


Figure 3: **Diffusivity for LGPS.** Lithium D^* is plotted as a function of $1000/T$ for LGPS ($\text{Li}_{10}\text{GeP}_2\text{S}_{12}$). (Left) $2 \times 2 \times 1$ supercell results from AIMD (25 ps training and ~ 150 ps full trajectories) and 150 ps LiFLOW inference. Shaded region represents 95% confidence intervals (CIs) for the Arrhenius fit ($1/T$ vs. $\log D^*(T)$) from 25 ps AIMD data. (Right) $4 \times 4 \times 4$ supercell results from fine-tuned MLIP and LiFLOW inference (1 ns).

Table 3: **Activation energies for LGPS.** Arrhenius fit based on the data in Fig. 3 (left).

Method	E_A [eV]	95% CI [eV]
AIMD (25 ps)	0.173	(0.141, 0.205)
AIMD (all)	0.192	(0.175, 0.205)
LiFLOW	0.185	(0.181, 0.190)

Table 4: **Prediction speed.** Time required to predict the 1 ns trajectory for LGPS ([†]extrapolated).

Method	Supercell	# atoms	Time
AIMD [†]	$2 \times 2 \times 1$	200	340 days
MLIP	$2 \times 2 \times 1$	200	5.8 hrs
LiFLOW	$2 \times 2 \times 1$	200	48 s
	$4 \times 4 \times 4$	3,200	352 s

²The negative log density, scaled by $k_B T$, $F(\mathbf{x}) = -k_B T \log p(\mathbf{x})$, is also known as the *potential of mean force* (PMF) or the *free energy surface* in the chemistry and physics literature.

Large-scale inference By modeling the distribution of atomic displacements, the generative model can naturally generalize across different supercell sizes, as indicated by the supercell invariance (Eq. (7)). We evaluated scalability and temperature transferability using a $4 \times 4 \times 4$ supercell, performing LiFLOW inference over 1,000 steps (1 ns), with the resulting D^* values presented in Fig. 3. For temperatures below the maximum training temperature (1400 K), the LiFLOW model generates stable trajectories that extend far beyond the 25 ps length of the training set trajectories (25 ps). When compared to the reference dynamics from Winter & Gómez-Bombarelli (2023) on LGPS, which used extensive simulations with a fine-tuned MLIP, D^* values predicted by LiFLOW closely match the reference values within the interpolative regime (i.e., the training temperature range). However, as we extend to lower T (higher $1000/T$) beyond the training range, D^* decreases much more slowly than the reference values (Fig. A3), indicating fictitious diffusive behavior when extrapolating to lower T . This behavior is expected, as the model was trained primarily on larger displacements of lithium atoms at higher T .

Computational cost The computation time for 1 ns of inference using the methods investigated in this paper is reported in Table 4. MLIP-based simulations significantly reduce the time required for materials simulations (days to hours), and the LiFLOW model accelerates this even further (hours to seconds). Even taking into account the training time of the LiFLOW model (\lesssim an hour), it remains significantly more efficient than AIMD simulations (see Appendix D.5). Given that AIMD scales as $\mathcal{O}(n^3)$ in theory, while both LiFLOW and MLIPs scale as $\mathcal{O}(n)$ for large systems (assuming graphs with radius cutoffs), the LiFLOW model enables efficient large-scale modeling of atomistic dynamics, as demonstrated in this work.

5 DISCUSSION

Conclusion and outlook We proposed the LiFLOW model, a generative acceleration framework designed to accelerate MD simulations for crystalline materials, with a focus on lithium SSEs. The model consists of two key components: a *Propagator*, which generates atomic displacements for time propagation, and a *Corrector*, which applies denoising. Both components utilize a conditional flow matching scheme, and we introduced a thermally and chemically adaptive prior based on the Maxwell–Boltzmann distribution and modified the PAINN model as a marginal flow approximator, both of which were critical for the accurate reproduction of dynamics. In our analysis of lithium-containing material trajectories, we consistently observed a Spearman rank correlation of 0.7–0.8 for lithium MSD in unseen compositions. This indicates the potential of the LiFLOW model for computational screening to identify materials with high lithium diffusivity. Furthermore, we demonstrated the ability to extend short-length accurate AIMD trajectories by training the LiFLOW model. This allowed us to infill insufficient observations, reproduce accurate temperature dependencies, and maintain high accuracy when scaling up to much larger supercells. Compared to simulations using MLIPs and AIMD, LiFLOW offers significant speedups of $400\times$ and $600,000\times$, respectively. This provides a practical means of scaling MD simulations to larger spatiotemporal domains.

Limitations and future directions First, although we have demonstrated the importance of designing the prior for the flow matching process, determining the appropriate prior scale remains a hyperparameter. A theoretical analysis of the optimal prior distribution would provide a more principled approach to designing priors tailored to specific acceleration tasks and material systems. This also applies to the choice of time step Δt : we used a fixed time step based on observation (Appendix A.3), but given the site-to-site hopping nature of atomistic transport, our method may benefit from adaptive or controllable time stepping (e.g., Schreiner et al. (2023)). Additionally, while LiFLOW performs well within the trained temperature range, it struggles to extrapolate beyond the training regime, where system dynamics may differ significantly from the training data. As a result, the current approach lacks the broad generalizability seen in universal MLIP models, which preserve the physical dynamics of systems while approximating the potential energy landscape. To improve reliability and develop a model capable of capturing emergent system behaviors, generative approaches would benefit from incorporating thermodynamic principles more explicitly (Tiwary et al., 2024; Dibak et al., 2022; Herron et al., 2023). Lastly, the accuracy of LiFLOW is inherently limited by the accuracy of the reference dynamics. Given the variety of MD simulation methods and their trade-offs between accuracy and speed, transfer learning or multi-fidelity frameworks could be considered for efficient training in practical applications.

REPRODUCIBILITY STATEMENT

The code and trajectory dataset necessary to reproduce the results will be made publicly available upon acceptance of this work. The sources of the external AIMD trajectories are provided in Appendix C.2.

ACKNOWLEDGMENTS

The authors thank Hoje Chun, Xiaochen Du, and MinGyu Choi for detailed feedback on the manuscript, Xiang Fu, Sungsoo Ahn, Johannes C. B. Dietschreit, and Mark Goldstein for their helpful suggestions and discussions, and Kacper Kapuśniak for providing the preliminary codebase for their work. We acknowledge the MIT SuperCloud and Lincoln Laboratory Supercomputing Center for providing HPC resources. J.N. acknowledges support from the Toyota Research Institute.

REFERENCES

- Mila AI4Science, Alex Hernandez-Garcia, Alexandre Duval, Alexandra Volokhova, Yoshua Bengio, Divya Sharma, Pierre Luc Carrier, Yasmine Benabed, Michał Koziarski, and Victor Schmidt. Crystal-GFN: sampling crystals with desirable properties and constraints, 2023. URL <https://arxiv.org/abs/2310.04925>. (cited on page 3)
- John Christopher Bachman, Sokseiha Muy, Alexis Grimaud, Hao-Hsun Chang, Nir Pour, Simon F Lux, Odysseas Paschos, Filippo Maglia, Saskia Lupart, Peter Lamp, Livia Giordano, and Yang Shao-Horn. Inorganic solid-state electrolytes for lithium batteries: Mechanisms and properties governing ion conduction. *Chem. Rev.*, 116(1):140–162, 2016. URL <https://doi.org/10.1021/acs.chemrev.5b00563>. (cited on page 1)
- Joseph E. Basconi and Michael R. Shirts. Effects of temperature control algorithms on transport properties and kinetics in molecular dynamics simulations. *J. Chem. Theory Comput.*, 9(7):2887–2899, 2013. URL <https://doi.org/10.1021/ct400109a>. (cited on page 16)
- Ilyes Batatia, Philipp Benner, Yuan Chiang, Alin M. Elena, Dávid P. Kovács, Janosh Riebesell, Xavier R. Advincula, Mark Asta, Matthew Avaylon, William J. Baldwin, Fabian Berger, Noam Bernstein, Arghya Bhowmik, Samuel M. Blau, Vlad Cărare, James P. Darby, Sandip De, Flaviano Della Pia, Volker L. Deringer, Rokas Elijošius, Zakariya El-Machachi, Fabio Falcioni, Edwin Fako, Andrea C. Ferrari, Annalena Genreith-Schriever, Janine George, Rhys E. A. Goodall, Clare P. Grey, Petr Grigorev, Shuang Han, Will Handley, Hendrik H. Heenen, Kersti Hermansson, Christian Holm, Jad Jaafar, Stephan Hofmann, Konstantin S. Jakob, Hyunwook Jung, Venkat Kapil, Aaron D. Kaplan, Nima Karimitari, James R. Kermode, Namu Kroupa, Jolla Kullgren, Matthew C. Kuner, Domantas Kuryla, Guoda Liepuoniute, Johannes T. Margraf, Ioan-Bogdan Magdău, Angelos Michaelides, J. Harry Moore, Aakash A. Naik, Samuel P. Niblett, Sam Walton Norwood, Niamh O’Neill, Christoph Ortner, Kristin A. Persson, Karsten Reuter, Andrew S. Rosen, Lars L. Schaaf, Christoph Schran, Benjamin X. Shi, Eric Sivonxay, Tamás K. Stenczel, Viktor Svahn, Christopher Sutton, Thomas D. Swinburne, Jules Tilly, Cas van der Oord, Eszter Varga-Umbrich, Tejs Vegge, Martin Vondrák, Yangshuai Wang, William C. Witt, Fabian Zills, and Gábor Csányi. A foundation model for atomistic materials chemistry, 2024. URL <https://arxiv.org/abs/2401.00096>. (cited on pages 2, 6, 18, 20, and 23)
- Bowen Deng, Peichen Zhong, KyuJung Jun, Janosh Riebesell, Kevin Han, Christopher J Bartel, and Gerbrand Ceder. CHGNet as a pretrained universal neural network potential for charge-informed atomistic modelling. *Nat. Mach. Intell.*, 5(9):1031–1041, 2023. URL <https://doi.org/10.1038/s42256-023-00716-3>. (cited on page 2)
- Bowen Deng, Yunyeong Choi, Peichen Zhong, Janosh Riebesell, Shashwat Anand, Zhuohan Li, KyuJung Jun, Kristin A. Persson, and Gerbrand Ceder. Overcoming systematic softening in universal machine learning interatomic potentials by fine-tuning, 2024. URL <https://arxiv.org/abs/2405.07105>. (cited on page 2)
- Manuel Dibak, Leon Klein, Andreas Krämer, and Frank Noé. Temperature steerable flows and boltzmann generators. *Phys. Rev. Research*, 4(4):L042005, 2022. URL <https://doi.org/10.1103/PhysRevResearch.4.L042005>. (cited on page 10)

- Matthias Fey and Jan Eric Lenssen. Fast graph representation learning with PyTorch Geometric, 2019. URL <https://arxiv.org/abs/1903.02428>. (cited on page 23)
- Daan Frenkel and Berend Smit. *Understanding Molecular Simulation: From Algorithms to Applications*. Elsevier, 3rd edition, 2023. (cited on page 2)
- Pascal Friederich, Florian Häse, Jonny Proppe, and Alán Aspuru-Guzik. Machine-learned potentials for next-generation matter simulations. *Nat. Mater.*, 20(6):750–761, 2021. URL <https://doi.org/10.1038/s41563-020-0777-6>. (cited on pages 1 and 2)
- Xiang Fu, Zhenghao Wu, Wujie Wang, Tian Xie, Sinan Ketten, Rafael Gomez-Bombarelli, and Tommi S. Jaakkola. Forces are not enough: Benchmark and critical evaluation for machine learning force fields with molecular simulations. *Transactions on Machine Learning Research*, 2023a. ISSN 2835-8856. URL <https://openreview.net/forum?id=A8pqQipwkt>. (cited on page 1)
- Xiang Fu, Tian Xie, Nathan J. Rebello, Bradley Olsen, and Tommi S. Jaakkola. Simulate time-integrated coarse-grained molecular dynamics with multi-scale graph networks. *Transactions on Machine Learning Research*, 2023b. ISSN 2835-8856. URL <https://openreview.net/forum?id=y8RZoPjEU1>. (cited on pages 1, 3, and 5)
- Jiaqi Guan, Xiangxin Zhou, Yuwei Yang, Yu Bao, Jian Peng, Jianzhu Ma, Qiang Liu, Liang Wang, and Quanquan Gu. DecompDiff: Diffusion models with decomposed priors for structure-based drug design. In Andreas Krause, Emma Brunskill, Kyunghyun Cho, Barbara Engelhardt, Sivan Sabato, and Jonathan Scarlett (eds.), *Proceedings of the 40th International Conference on Machine Learning*, volume 202 of *Proceedings of Machine Learning Research*, pp. 11827–11846. PMLR, 23–29 Jul 2023. URL <https://proceedings.mlr.press/v202/guan23a.html>. (cited on page 3)
- Jürgen Hafner. Ab-initio simulations of materials using VASP: Density-functional theory and beyond. *J. Comput. Chem.*, 29(13):2044–2078, 2008. URL <https://doi.org/10.1002/jcc.21057>. (cited on page 23)
- Xingfeng He, Yizhou Zhu, Alexander Epstein, and Yifei Mo. Statistical variances of diffusional properties from ab initio molecular dynamics simulations. *npj Comput. Mater.*, 4(1):18, 2018. URL <https://doi.org/10.1038/s41524-018-0074-y>. (cited on page 17)
- Lukas Herron, Kinjal Mondal, John S. Schneckloth, and Pratyush Tiwary. Inferring phase transitions and critical exponents from limited observations with thermodynamic maps, 2023. URL <https://arxiv.org/abs/2308.14885>. (cited on page 10)
- William G Hoover. Canonical dynamics: Equilibrium phase-space distributions. *Phys. Rev. A*, 31(3):1695–1697, 1985. URL <https://doi.org/10.1103/PhysRevA.31.1695>. (cited on pages 16 and 18)
- Tim Hsu, Babak Sadigh, Vasily Bulatov, and Fei Zhou. Score dynamics: Scaling molecular dynamics with picoseconds time steps via conditional diffusion model. *J. Chem. Theory Comput.*, 20(6):2335–2348, 2024. URL <https://doi.org/10.1021/acs.jctc.3c01361>. (cited on pages 1 and 3)
- Ross Irwin, Alessandro Tibo, Jon Paul Janet, and Simon Olsson. Efficient 3d molecular generation with flow matching and scale optimal transport, 2024. URL <https://arxiv.org/abs/2406.07266>. (cited on page 3)
- Anubhav Jain, Shyue Ping Ong, Geoffroy Hautier, Wei Chen, William Davidson Richards, Stephen Dacek, Shreyas Cholia, Dan Gunter, David Skinner, Gerbrand Ceder, and Kristin A. Persson. Commentary: The Materials Project: A materials genome approach to accelerating materials innovation. *APL Mater.*, 1(1):011002, 2013. URL <https://doi.org/10.1063/1.4812323>. (cited on pages 6 and 18)
- Rui Jiao, Wenbing Huang, Peijia Lin, Jiaqi Han, Pin Chen, Yutong Lu, and Yang Liu. Crystal structure prediction by joint equivariant diffusion. In A. Oh, T. Naumann, A. Globerson, K. Saenko, M. Hardt, and S. Levine (eds.), *Advances in Neural Information Processing Systems*, volume 36, pp. 17464–17497. Curran Associates,

- Inc., 2023. URL https://proceedings.neurips.cc/paper_files/paper/2023/file/38b787fc530d0b31825827e2cc306656-Paper-Conference.pdf. (cited on page 3)
- Bowen Jing, Ezra Erives, Peter Pao-Huang, Gabriele Corso, Bonnie Berger, and Tommi Jaakkola. EigenFold: Generative protein structure prediction with diffusion models, 2023. URL <https://arxiv.org/abs/2304.02198>. (cited on page 3)
- KyuJung Jun, Yingzhi Sun, Yihan Xiao, Yan Zeng, Ryounghee Kim, Haegyeom Kim, Lincoln J Miara, Dongmin Im, Yan Wang, and Gerbrand Ceder. Lithium superionic conductors with corner-sharing frameworks. *Nat. Mater.*, 21(8):924–931, 2022. URL <https://doi.org/10.1038/s41563-022-01222-4>. (cited on page 16)
- KyuJung Jun, Yu Chen, Grace Wei, Xiaochen Yang, and Gerbrand Ceder. Diffusion mechanisms of fast lithium-ion conductors. *Nat. Rev. Mater.*, 2024a. URL <https://doi.org/10.1038/s41578-024-00715-9>. (cited on page 16)
- KyuJung Jun, Byungju Lee, Ronald L. Kam, and Gerbrand Ceder. The nonexistence of a paddlewheel effect in superionic conductors. *Proc. Natl. Acad. Sci. U.S.A.*, 121(18):e2316493121, 2024b. URL <https://doi.org/10.1073/pnas.2316493121>. (cited on pages 6 and 19)
- Noriaki Kamaya, Kenji Homma, Yuichiro Yamakawa, Masaaki Hirayama, Ryoji Kanno, Masao Yonemura, Takashi Kamiyama, Yuki Kato, Shigenori Hama, Koji Kawamoto, and Akio Mitsui. A lithium superionic conductor. *Nat. Mater.*, 10(9):682–686, 2011. URL <https://doi.org/10.1038/nmat3066>. (cited on page 19)
- Takuya Kimura, Takeaki Inaoka, Ryo Izawa, Takumi Nakano, Chie Hotehama, Atsushi Sakuda, Masahiro Tatsumisago, and Akitoshi Hayashi. Stabilizing high-temperature α -Li₃PS₄ by rapidly heating the glass. *J. Am. Chem. Soc.*, 145(26):14466–14474, 2023. URL <https://doi.org/10.1021/jacs.3c03827>. (cited on page 19)
- Diederik P. Kingma and Jimmy Ba. Adam: A method for stochastic optimization, 2014. URL <https://arxiv.org/abs/1412.6980>. (cited on page 22)
- Leon Klein, Andrew Foong, Tor Fjelde, Bruno Mlodozieniec, Marc Brockschmidt, Sebastian Nowozin, Frank Noe, and Ryota Tomioka. Timewarp: Transferable acceleration of molecular dynamics by learning time-coarsened dynamics. In A. Oh, T. Naumann, A. Globerson, K. Saenko, M. Hardt, and S. Levine (eds.), *Advances in Neural Information Processing Systems*, volume 36, pp. 52863–52883. Curran Associates, Inc., 2023a. URL <https://openreview.net/forum?id=EjMLpTgvKH>. (cited on pages 1 and 3)
- Leon Klein, Andreas Krämer, and Frank Noe. Equivariant flow matching. In A. Oh, T. Naumann, A. Globerson, K. Saenko, M. Hardt, and S. Levine (eds.), *Advances in Neural Information Processing Systems*, volume 36. Curran Associates, Inc., 2023b. URL https://proceedings.neurips.cc/paper_files/paper/2023/file/bc827452450356f9f558f4e4568d553b-Paper-Conference.pdf. (cited on page 4)
- Tsz Wai Ko and Shyue Ping Ong. Recent advances and outstanding challenges for machine learning interatomic potentials. *Nat. Comput. Sci.*, 3(12):998–1000, 2023. URL <https://doi.org/10.1038/s43588-023-00561-9>. (cited on pages 1 and 2)
- Jonas Köhler, Leon Klein, and Frank Noe. Equivariant flows: Exact likelihood generative learning for symmetric densities. In Hal Daumé III and Aarti Singh (eds.), *Proceedings of the 37th International Conference on Machine Learning*, volume 119 of *Proceedings of Machine Learning Research*, pp. 5361–5370. PMLR, 13–18 Jul 2020. URL <https://proceedings.mlr.press/v119/kohler20a.html>. (cited on pages 4 and 17)
- W. Kohn and L. J. Sham. Self-consistent equations including exchange and correlation effects. *Phys. Rev.*, 140:A1133–A1138, 1965. URL <https://doi.org/10.1103/PhysRev.140.A1133>. (cited on page 16)
- Ask Hjorth Larsen, Jens Jørgen Mortensen, Jakob Blomqvist, Ivano E Castelli, Rune Christensen, Marcin Dułak, Jesper Friis, Michael N Groves, Bjørk Hammer, Cory Hargus, Eric D Hermes,

- Paul C Jennings, Peter Bjerre Jensen, James Kermode, John R Kitchin, Esben Leonhard Kolsbjerg, Joseph Kubal, Kristen Kaasbjerg, Steen Lysgaard, Jón Bergmann Maronsson, Tristan Maxson, Thomas Olsen, Lars Pastewka, Andrew Peterson, Carsten Rostgaard, Jakob Schjøtz, Ole Schütt, Mikkel Strange, Kristian S Thygesen, Tejs Vegge, Lasse Vilhelmsen, Michael Walter, Zhenhua Zeng, and Karsten W Jacobsen. The atomic simulation environment—a python library for working with atoms. *J. Phys.: Condens. Matter*, 29(27):273002, 2017. URL <https://doi.org/10.1088/1361-648X/aa680e>. (cited on pages 18 and 23)
- Byungju Lee, KyuJung Jun, Bin Ouyang, and Gerbrand Ceder. Weak correlation between the polyanion environment and ionic conductivity in amorphous Li–P–S superionic conductors. *Chem. Mater.*, 35(3):891–899, 2023. URL <https://doi.org/10.1021/acs.chemmater.2c02458>. (cited on page 19)
- Sang-gil Lee, Heeseung Kim, Chaehun Shin, Xu Tan, Chang Liu, Qi Meng, Tao Qin, Wei Chen, Sungroh Yoon, and Tie-Yan Liu. PriorGrad: Improving conditional denoising diffusion models with data-dependent adaptive prior. In *International Conference on Learning Representations*, 2022. URL <https://openreview.net/forum?id=BNiN4IjC5>. (cited on page 3)
- Yaron Lipman, Ricky T. Q. Chen, Heli Ben-Hamu, Maximilian Nickel, and Matthew Le. Flow matching for generative modeling. In *The Eleventh International Conference on Learning Representations*, 2023. URL <https://openreview.net/forum?id=PqvMRDCJT9t>. (cited on page 2)
- Cibrán López, Riccardo Rurali, and Claudio Cazorla. How concerted are ionic hops in inorganic solid-state electrolytes? *J. Am. Chem. Soc.*, 146(12):8269–8279, 2024. URL <https://doi.org/10.1021/jacs.3c13279>. (cited on pages 6 and 19)
- Edward J. Maginn, Richard A. Messerly, Daniel J. Carlson, Daniel R. Roe, and J. Richard Elliot. Best practices for computing transport properties 1. self-diffusivity and viscosity from equilibrium molecular dynamics [article v1.0]. *Living Journal of Computational Molecular Science*, 1(1):6324, 2018. URL <https://doi.org/10.33011/livecoms.1.1.6324>. (cited on page 16)
- Arumugam Manthiram, Xingwen Yu, and Shaofei Wang. Lithium battery chemistries enabled by solid-state electrolytes. *Nat. Rev. Mater.*, 2(4):1–16, 2017. URL <https://doi.org/10.1038/natrevmats.2016.103>. (cited on page 16)
- Dominik Marx and Jürg Hutter. *Ab Initio Molecular Dynamics: Basic Theory and Advanced Methods*. Cambridge University Press, 2009. (cited on page 16)
- Andrew R. McCluskey, Samuel W. Coles, and Benjamin J. Morgan. Accurate estimation of diffusion coefficients and their uncertainties from computer simulation, 2024a. URL <https://arxiv.org/abs/2305.18244>. (cited on page 7)
- Andrew R. McCluskey, Alexander G. Squires, Josh Dunn, Samuel W. Coles, and Benjamin J. Morgan. kinisi: Bayesian analysis of mass transport from molecular dynamics simulations. *J. Open Source Softw.*, 9(94):5984, 2024b. URL <https://doi.org/10.21105/joss.05984>. (cited on pages 7 and 23)
- Benjamin Kurt Miller, Ricky T. Q. Chen, Anuroop Sriram, and Brandon M Wood. FlowMM: Generating materials with Riemannian flow matching. In Ruslan Salakhutdinov, Zico Kolter, Katherine Heller, Adrian Weller, Nuria Oliver, Jonathan Scarlett, and Felix Berkenkamp (eds.), *Proceedings of the 41st International Conference on Machine Learning*, volume 235 of *Proceedings of Machine Learning Research*, pp. 35664–35686. PMLR, 21–27 Jul 2024. URL <https://proceedings.mlr.press/v235/miller24a.html>. (cited on page 3)
- Shuichi Nosé. A unified formulation of the constant temperature molecular dynamics methods. *J. Chem. Phys.*, 81(1):511–519, 1984. URL <https://doi.org/10.1063/1.447334>. (cited on pages 16 and 18)
- Adam Paszke, Sam Gross, Francisco Massa, Adam Lerer, James Bradbury, Gregory Chanan, Trevor Killeen, Zeming Lin, Natalia Gimelshein, Luca Antiga, Alban Desmaison, Andreas Kopf, Edward Yang, Zachary DeVito, Martin Raison, Alykhan Tejani, Sasank Chilamkurthy, Benoit Steiner, Lu Fang, Junjie Bai, and Soumith Chintala. PyTorch: An imperative style, high-performance

- deep learning library. In H. Wallach, H. Larochelle, A. Beygelzimer, F. d'Alché-Buc, E. Fox, and R. Garnett (eds.), *Advances in Neural Information Processing Systems*, volume 32, pp. 8026–8037. Curran Associates, Inc., 2019. URL https://proceedings.neurips.cc/paper_files/paper/2019/file/bdbca288fee7f92f2bfa9f7012727740-Paper.pdf. (cited on page 23)
- Aram-Alexandre Pooladian, Heli Ben-Hamu, Carles Domingo-Enrich, Brandon Amos, Yaron Lipman, and Ricky T. Q. Chen. Multisample flow matching: Straightening flows with minibatch couplings. In Andreas Krause, Emma Brunskill, Kyunghyun Cho, Barbara Engelhardt, Sivan Sabato, and Jonathan Scarlett (eds.), *Proceedings of the 40th International Conference on Machine Learning*, volume 202 of *Proceedings of Machine Learning Research*, pp. 28100–28127. PMLR, 23–29 Jul 2023. URL <https://proceedings.mlr.press/v202/pooladian23a.html>. (cited on page 5)
- Mathias Schreiner, Ole Winther, and Simon Olsson. Implicit transfer operator learning: Multiple time-resolution models for molecular dynamics. In A. Oh, T. Naumann, A. Globerson, K. Saenko, M. Hardt, and S. Levine (eds.), *Advances in Neural Information Processing Systems*, volume 36, pp. 36449–36462. Curran Associates, Inc., 2023. URL <https://openreview.net/forum?id=1kZx7JiuA2>. (cited on pages 1, 3, 10, and 20)
- Kristof Schütt, Pieter-Jan Kindermans, Huziel Enoc Saucedo Felix, Stefan Chmiela, Alexandre Tkatchenko, and Klaus-Robert Müller. SchNet: A continuous-filter convolutional neural network for modeling quantum interactions. In I. Guyon, U. Von Luxburg, S. Bengio, H. Wallach, R. Fergus, S. Vishwanathan, and R. Garnett (eds.), *Advances in Neural Information Processing Systems*, volume 30. Curran Associates, Inc., 2017. URL https://proceedings.neurips.cc/paper_files/paper/2017/file/303ed4c69846ab36c2904d3ba8573050-Paper.pdf. (cited on page 2)
- Kristof Schütt, Oliver Unke, and Michael Gastegger. Equivariant message passing for the prediction of tensorial properties and molecular spectra. In Marina Meila and Tong Zhang (eds.), *Proceedings of the 38th International Conference on Machine Learning*, volume 139 of *Proceedings of Machine Learning Research*, pp. 9377–9388. PMLR, 18–24 Jul 2021. URL <https://proceedings.mlr.press/v139/schutt21a.html>. (cited on pages 5 and 20)
- Pratyush Tiwary, Lukas Herron, Richard John, Suemin Lee, Disha Sanwal, and Ruiyu Wang. Generative artificial intelligence for computational chemistry: a roadmap to predicting emergent phenomena, 2024. URL <https://arxiv.org/abs/2409.03118>. (cited on page 10)
- Yan Wang, William Davidson Richards, Shyue Ping Ong, Lincoln J Miara, Jae Chul Kim, Yifei Mo, and Gerbrand Ceder. Design principles for solid-state lithium superionic conductors. *Nat. Mater.*, 14(10):1026–1031, 2015. URL <https://doi.org/10.1038/nmat4369>. (cited on page 16)
- Gavin Winter and Rafael Gómez-Bombarelli. Simulations with machine learning potentials identify the ion conduction mechanism mediating non-arrhenius behavior in Igps. *J. Phys.: Energy*, 5(2): 024004, 2023. URL <https://doi.org/10.1088/2515-7655/acbbef>. (cited on page 10)
- Tian Xie, Xiang Fu, Octavian-Eugen Ganea, Regina Barzilay, and Tommi S. Jaakkola. Crystal diffusion variational autoencoder for periodic material generation. In *International Conference on Learning Representations*, 2022. URL <https://openreview.net/forum?id=03RLpj-tc..> (cited on page 3)
- Sherry Yang, KwangHwan Cho, Amil Merchant, Pieter Abbeel, Dale Schuurmans, Igor Mordatch, and Ekin Dogus Cubuk. Scalable diffusion for materials generation. In *The Twelfth International Conference on Learning Representations*, 2024. URL <https://openreview.net/forum?id=wm4WlHoXpC>. (cited on page 3)
- Ziyang Yu, Wenbing Huang, and Yang Liu. Force-guided bridge matching for full-atom time-coarsened dynamics of peptides, 2024. URL <https://arxiv.org/abs/2408.15126>. (cited on pages 1 and 3)
- Claudio Zeni, Robert Pinsler, Daniel Zügner, Andrew Fowler, Matthew Horton, Xiang Fu, Sasha Shysheya, Jonathan Crabbé, Lixin Sun, Jake Smith, Bichlien Nguyen, Hannes Schulz, Sarah Lewis, Chin-Wei Huang, Ziheng Lu, Yichi Zhou, Han Yang, Hongxia Hao, Jielan Li, Ryota Tomioka, and Tian Xie. MatterGen: a generative model for inorganic materials design, 2024. URL <https://arxiv.org/abs/2312.03687>. (cited on page 3)

A ADDITIONAL BACKGROUND

A.1 SOLID-STATE ELECTROLYTES

While lithium-ion diffusion in most solid-state materials is generally slow, solid-state electrolytes are a special class of materials in which lithium ions can undergo fast diffusion, often referred to as superionic conductors (Manthiram et al., 2017; Jun et al., 2024a). They serve as a key component for all-solid-state batteries, where enhanced safety is anticipated by replacing flammable organic liquid electrolytes with solid-state alternatives. A major class of solid electrolytes discussed in this work consists of inorganic crystalline materials, which have long-range atomic ordering. In most of these inorganic crystalline solid electrolytes, the anions (Wang et al., 2015) and the non-lithium cations (Jun et al., 2022) remain immobile, selectively permitting the translational motion of the lithium ions. This allows lithium ions to percolate through the crystal structure with a flat energy landscape (or low migration barrier), resulting in a high diffusion coefficient and ionic conductivity.

A.2 AIMD SIMULATION

Ab initio MD AIMD simulations are typically carried out using the Born–Oppenheimer molecular dynamics (BOMD) approach (Marx & Hutter, 2009), as defined with the following equation of motion (Eq. (15)) and the time-independent Schrödinger equation (Eq. (16)):

$$M\ddot{\mathbf{X}} = -\nabla_{\mathbf{X}} \min_{\Psi_0} \langle \Psi_0 | \mathcal{H}(\mathbf{X}) | \Psi_0 \rangle, \quad (15)$$

$$E_0 \Psi_0 = \mathcal{H}(\mathbf{X}) \Psi_0, \quad (16)$$

where $\mathcal{H}(\mathbf{X})$ represents the electronic Hamiltonian, Ψ_0 is the ground state wavefunction, and $\langle \Psi_0 | \mathcal{H}(\mathbf{X}) | \Psi_0 \rangle$ denotes the quantum mechanical expectation value. At each time step, the ground state wavefunction is obtained by solving Eq. (16), after which the forces are computed as a derivative of the ground state energy with respect to atomic coordinates (Eq. (15)).

For crystalline materials, Eq. (16) is typically solved using Kohn–Sham density functional theory (DFT, Kohn & Sham (1965)), where the ground state energy is expressed as

$$\min_{\Psi_0} \langle \Psi_0 | \mathcal{H}(\mathbf{X}) | \Psi_0 \rangle = \min_{\{\phi_i\}} E^{\text{KS}}[\{\phi_i\}; \mathbf{X}] \quad (17)$$

with E^{KS} being the Kohn–Sham energy functional and $\{\phi_i\}$ denoting a set of auxiliary functions called Kohn–Sham orbitals, which depend on the electron positions. The functional optimization in Eq. (17) is equivalent to solving the set of coupled Kohn–Sham equations $H^{\text{KS}} \phi_i = \epsilon_i \phi_i$, where H^{KS} is the one-particle Hamiltonian and $\{\epsilon_i\}$ are the Kohn–Sham eigenvalues. Solving these eigenvalue equations, which involves diagonalizing the Hamiltonian, scales as $\mathcal{O}(n^3)$ with respect to the system size n , defined by the number of atoms (as in the main text) or electrons.

Thermostat choice To maintain a constant temperature T in the system, the dynamics is coupled with an external control mechanism known as a thermostat. We used Nosé–Hoover thermostat (Nosé, 1984; Hoover, 1985) for dataset generation. To avoid thermostat-dependent dynamical artifacts, velocity *scaling* thermostats (e.g., Berendsen, Nosé–Hoover, and stochastic velocity rescaling) should be used instead of velocity *randomization* thermostats (e.g., Langevin and Andersen). The latter may lead to reduced diffusivity values due to rapid decorrelation of velocities (Basconi & Shirts, 2013).

A.3 TASK DESIGN

Fixing the volume In AIMD simulations for solid electrolytes, or in general when modeling the transport properties of atomistic systems, simulations are typically conducted under the NVT (constant volume) ensemble. Although real materials are often under constant pressure conditions, employing a barostat in simulations to control pressure modifies cell volume, potentially leading to significant changes in particle positions and dynamics (Maginn et al., 2018). In practice, AIMD simulations are initiated after energy minimization of the material structure (with respect to both atomic coordinates and cell dimensions) under the assumption that thermal expansion of the cell does not significantly affect the transport properties.

Unwrapped coordinates In atomistic systems with periodic boundary conditions (PBCs), particles that exit one side of the simulation box effectively reenter from the opposite side. A straightforward way to handle this is to use *wrapped* coordinates, where the positions are continuously confined within the simulation box. However, this introduces jumps in atomic positions during long-range motions, which can distort the calculation of kinetic properties such as MSD and diffusivity. To avoid this, the coordinates must be *unwrapped* before computing such properties. Alternatively, particle positions can be propagated using unwrapped coordinates from the start, without wrapping them back when crossing the cell boundaries.

It is possible to unwrap trajectories during the post-processing of AIMD simulations, assuming that no particles move more than half the cell dimensions between time steps. This condition generally holds for typical AIMD simulations, which use small time steps. However, in the case of LiFLOW modeling in this work, particle displacements can exceed half the box size because (1) we simulate with a much larger time step $\Delta\tau$, and (2) AIMD simulation cells are typically small due to high computational costs (see Appendix A.2). Hence, we use unwrapped coordinates directly when formulating the displacement modeling task for LiFLOW.

Choice of $\Delta\tau$ Since the goal of generative displacement modeling in this work is to efficiently accelerate MD simulations, the propagation time step $\Delta\tau$ must be significantly larger than the MD time step $\delta\tau$. However, due to the high cost of generating data, $\Delta\tau$ should not be so large that the modes of atomic displacements are not adequately covered by the training set trajectories.

To determine $\Delta\tau$, we consider the time evolution of lithium MSD for typical lithium-ion solid-state electrolytes. For small $\Delta\tau$ values (< 0.1 ps), the MSD grows approximately as $\text{MSD} \propto \Delta\tau^{1.42}$, reflecting the ballistic and vibrational motion of lithium ions (He et al., 2018). In this regime, the benefit of generative modeling is limited, as the evolution of atomic positions is closely related to the initial velocities. For larger $\Delta\tau$ ($\gtrsim 1$ ps), the MSD grows linearly as $\text{MSD} \propto \Delta\tau$, indicating the onset of diffusive motion, as described by Eq. (13). Given that our training trajectories span 25 ps, we select $\Delta\tau = 1$ ps to ensure that the generative model captures a diverse range of displacement modes present in the training data.

Units The atomic unit system is adopted in this work. Unless stated otherwise, the units are as follows: length is in Å, temperature in K, mass in atomic mass units (u), and energy in eV. For example, the scaling factor for the Maxwell–Boltzmann prior has an implied unit of Å · (eV · K/u) $^{-1/2}$ for converting $(k_B T/m)^{1/2}$ into positions.

B PROOF FOR PROPOSITION 1

Proposition 1 *Given an invariant base distribution $p_0(\mathbf{D}_0)$ satisfying Eqs. (3) and (6) and an equivariant conditional vector field $u_t(\mathbf{D}_t|\mathbf{D}_1)$ with the following properties:*

$$u_t(\mathbf{P}\mathbf{D}_t|\mathbf{P}\mathbf{D}_1, \mathbf{P}\mathbf{X}, \mathbf{L}, \mathbf{P}\mathbf{a}, T) = \mathbf{P}u_t(\mathbf{D}_t|\mathbf{D}_1, \mathbf{X}, \mathbf{L}, \mathbf{a}, T), \quad \mathbf{P} \in S_n \quad (18)$$

$$u_t(\mathbf{D}_t\mathbf{R}|\mathbf{D}_1\mathbf{R}, \mathbf{X}\mathbf{R}, \mathbf{L}\mathbf{R}, \mathbf{a}, T) = u_t(\mathbf{D}_t|\mathbf{D}_1, \mathbf{X}, \mathbf{L}, \mathbf{a}, T)\mathbf{R}, \quad \mathbf{R} \in \text{O}(3) \quad (19)$$

the generated conditional probability path $p_{t|1}(\mathbf{D}_t|\mathbf{D}_1)$ is invariant. Furthermore, given that the data distribution $q(\mathbf{D}_1)$ is invariant, the marginal probability path $p_t(\mathbf{D}_t)$ is also invariant.

Proof. We will prove for the O(3) symmetry, with a similar approach applying to S_n . We omit the conditional variables $(\mathbf{X}, \mathbf{L}, \mathbf{a}, T)$, as their transformations under group actions are implied by those of \mathbf{D}_1 , either remaining invariant or transforming equivariantly. The first part of the proof follows from Theorems 1 and 2 in Köhler et al. (2020), with additional conditional variables. The conditional flow generated by the conditional vector field is

$$\psi_t(\mathbf{D}_0|\mathbf{D}_1) = \mathbf{D}_0 + \int_0^t u_s(\mathbf{D}_s|\mathbf{D}_1) ds. \quad (20)$$

Now, we apply $\mathbf{R} \in \text{O}(3)$:

$$\begin{aligned}
\psi_t(\mathbf{D}_0 \mathbf{R} | \mathbf{D}_1 \mathbf{R}) &= \mathbf{D}_0 \mathbf{R} + \int_0^t u_s(\mathbf{D}_s \mathbf{R} | \mathbf{D}_1 \mathbf{R}) \, ds \\
&= \mathbf{D}_0 \mathbf{R} + \int_0^t u_s(\mathbf{D}_s | \mathbf{D}_1) \mathbf{R} \, ds \\
&= \left(\mathbf{D}_0 + \int_0^t u_s(\mathbf{D}_s | \mathbf{D}_1) \, ds \right) \mathbf{R} \\
&= \psi_t(\mathbf{D}_0 | \mathbf{D}_1) \mathbf{R}.
\end{aligned} \tag{21}$$

Thus, the conditional flow ψ_t is also equivariant with respect to \mathbf{R} . Now, the conditional probability path $p_{t|1}(\mathbf{D}_t | \mathbf{D}_1)$ is obtained as the pushforward of the prior distribution p_0 under ψ_t :

$$p_{t|1}(\mathbf{D}_t | \mathbf{D}_1) = [\psi_t]_{\#} p_0(\mathbf{D}_0) = p_0(\psi_t^{-1}(\mathbf{D}_t | \mathbf{D}_1)) \left| \det \frac{\partial \psi_t^{-1}}{\partial \mathbf{D}_t}(\mathbf{D}_t | \mathbf{D}_1) \right|. \tag{22}$$

Again, we apply $\mathbf{R} \in \text{O}(3)$:

$$\begin{aligned}
p_{t|1}(\mathbf{D}_t \mathbf{R} | \mathbf{D}_1 \mathbf{R}) &= p_0(\psi_t^{-1}(\mathbf{D}_t \mathbf{R} | \mathbf{D}_1 \mathbf{R})) \left| \det \frac{\partial \psi_t^{-1}}{\partial (\mathbf{D}_t \mathbf{R})}(\mathbf{D}_t \mathbf{R} | \mathbf{D}_1 \mathbf{R}) \right| \\
&= p_0(\psi_t^{-1}(\mathbf{D}_t | \mathbf{D}_1) \mathbf{R}) \left| \det \frac{\partial \psi_t^{-1}}{\partial (\mathbf{D}_t \mathbf{R})}(\mathbf{D}_t \mathbf{R} | \mathbf{D}_1 \mathbf{R}) \right| \\
&= p_0(\psi_t^{-1}(\mathbf{D}_t | \mathbf{D}_1)) \left| \det \mathbf{I}_n \otimes \mathbf{R} \right| \left| \det \frac{\partial \psi_t^{-1}}{\partial \mathbf{D}_t}(\mathbf{D}_t | \mathbf{D}_1) \right| \left| \det \mathbf{I}_n \otimes \mathbf{R} \right|^{-1} \\
&= p_0(\psi_t^{-1}(\mathbf{D}_t | \mathbf{D}_1)) \left| \det \frac{\partial \psi_t^{-1}}{\partial \mathbf{D}_t}(\mathbf{D}_t | \mathbf{D}_1) \right| \\
&= p_{t|1}(\mathbf{D}_t | \mathbf{D}_1),
\end{aligned} \tag{23}$$

where we used the fact that $|\det \mathbf{I}_n \otimes \mathbf{R}| = |\det \mathbf{R}|^n = 1$. Therefore, the resulting conditional probability path $p_{t|1}$ is also invariant with respect to \mathbf{R} .

Now, for the marginal probability $p_t(\mathbf{D}_t) = \int p_{t|1}(\mathbf{D}_t | \mathbf{D}_1) q(\mathbf{D}_1) \, d\mathbf{D}_1$,

$$\begin{aligned}
p_t(\mathbf{D}_t \mathbf{R}) &= \int p_{t|1}(\mathbf{D}_t \mathbf{R} | \mathbf{D}_1 \mathbf{R}) q(\mathbf{D}_1 \mathbf{R}) \, d(\mathbf{D}_1 \mathbf{R}) \\
&= \int p_{t|1}(\mathbf{D}_t | \mathbf{D}_1) q(\mathbf{D}_1) \left| \det \mathbf{I}_n \otimes \mathbf{R} \right| \, d\mathbf{D}_1 \\
&= \int p_{t|1}(\mathbf{D}_t | \mathbf{D}_1) q(\mathbf{D}_1) \, d\mathbf{D}_1 \\
&= p_t(\mathbf{D}_t),
\end{aligned} \tag{24}$$

which concludes the proof of the invariance of the marginal p_t . \square

C DATASET DETAILS

C.1 UNIVERSAL DATASET

We fetched 4,186 lithium-containing structures from Materials Project (Jain et al., 2013) with the criteria of (1) more than 10% of the atoms are lithium, (2) band gap > 2 eV, and (3) energy over the convex hull < 0.1 eV/atom. These criteria are designed to sample various modes of lithium-ion dynamics across different compositions, while maintaining minimal requirements for the solid-state electrolytes. After building a supercell of the structure in order to ensure that each dimension is larger than 9 Å and minimizing the structure, we conducted NVT MD simulations with MACE-MP-0 small model (Batatia et al., 2024) at 600, 800, 1000, and 1200 K for each structure. The initial velocities were assigned according to the temperature, and the system was propagated for 25 ps with the time step of 1 fs (25,000 steps) using Nosé–Hoover dynamics (Nosé, 1984; Hoover, 1985) as implemented in ASE (Larsen et al., 2017). We recorded the atom positions every ten steps.

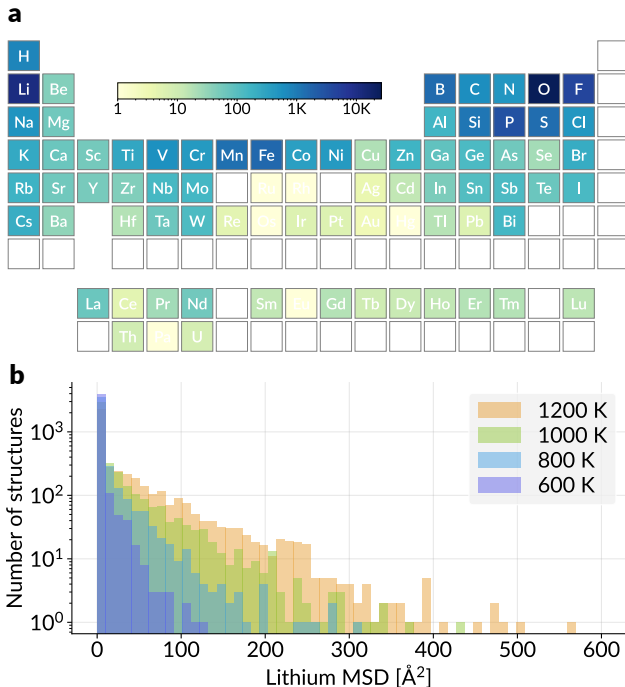


Figure A1: **Dataset statistics.** (a) Elemental count distribution across the unit cells of the structures in the dataset. (b) Histogram of lithium MSD values from 25-ps MD simulations at different temperatures.

C.2 AIMD DATASETS

LPS dataset Among the three LPS polymorphs, α - and β -LPS are fast lithium-ion conductors that remain stable at high temperatures, whereas the γ -phase is a slower lithium-ion conductor (Kimura et al., 2023; Lee et al., 2023). These polymorphs provide an excellent system to evaluate the capability of our model, as their crystal structures are quite similar—primarily differentiated by the orientation of the PS_4 tetrahedra and the corresponding lithium-ion sites—yet they exhibit drastically different lithium transport properties. We obtained the LPS trajectories from Jun et al. (2024b) directly from the authors. Supercell sizes of $2 \times 2 \times 2$, $1 \times 2 \times 2$, and $2 \times 2 \times 2$ were used for α -, β -, and γ - Li_3PS_4 , respectively. For each structure, five trajectories at temperatures of 600, 650, 700, 750, and 800 K were used. The reference trajectories used a time step of $\delta\tau = 2$ fs, which we subsampled every five steps to reduce redundancy in the training and test datasets. We set the LIFLOW time step $\Delta\tau$ to 500 steps (1 ps).

LGPS dataset LGPS is a prototypical lithium superionic conductor discovered in 2011 (Kamaya et al., 2011). We utilized AIMD trajectories for LGPS from López et al. (2024), accessible at <https://superionic.upc.edu/>. The reference simulations employed a time step of $\delta\tau = 1.5$ fs, with snapshots recorded every ten steps (15 fs). To align with this, we set the LIFLOW time step $\Delta\tau$ to 670 steps (1.005 ps).

D MODEL AND TRAINING

D.1 PRIOR SELECTOR

The prior selector model $\sigma_{\mathcal{S}}(\mathcal{M}_0, T)$ for species \mathcal{S} (lithium or frame) is a binary classifier that predicts whether the atom of the given species \mathcal{S} will exhibit large or small displacements based on the initial structure of materials. The same training and test splits were used for the universal dataset. Labels for large and small displacements were determined by the criterion $\text{MSD}_{\mathcal{S}}/\tau < 0.1 \text{ \AA}^2/\text{ps}$, computed over the reference simulation ($\tau = 25$ ps). The input features for the classifier are the atomic invariant features (128 dimensions) averaged over atoms of \mathcal{S} , extracted from a pre-trained

MACE-MP-0 small model (Batatia et al., 2024) given the initial structure $(\mathbf{X}_0, \mathbf{L}, \mathbf{a})$, along with the temperature $(T/1000 \text{ K}, \text{ a scalar})$. These features are concatenated and fed into a multi-layer perceptron with hidden layers of size 32 and 16, which is trained on the training set materials. The histograms of the MSD_S/τ distribution annotated with predicted labels are reported in Fig. A2.

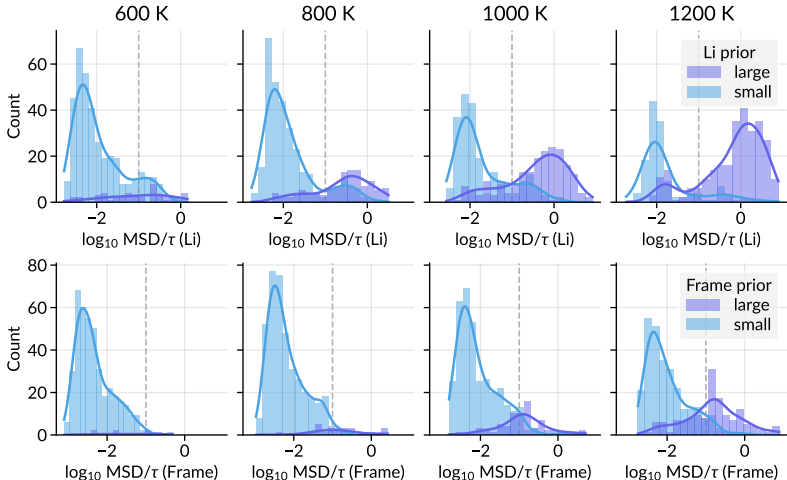


Figure A2: **Prior selector model performance.** Histogram of the target values, $\log_{10}(\text{MSD}_S/\tau)$, for lithium and frame atoms, colored by the predicted prior scale (small or large) for the test set materials. The intended classification threshold (-1.0) is marked by a vertical dotted line.

D.2 FLOW MODEL ARCHITECTURE

We adapt the PAINN model (Schütt et al., 2021) to parametrize the marginal flow approximator $v_\theta(\mathbf{D}_t|\mathbf{X}_\tau, \mathbf{L}, \mathbf{a}, T)$ for both the *Propagator* and *Corrector*. Schreiner et al. (2023) employed a modified version of the PAINN model, named CHIROPAINN, for a similar task for small biomolecules, introducing cross products during message passing in order to break reflection symmetry. Their modification was necessary due to their use of coarse-grained protein representation (C_α coordinates), where the mirror image of a C_α trace does not correspond to the mirror image of the full-atom structure. In contrast, we represent the material structure using all atomic coordinates without coarse-graining, preserving the reflection symmetry of the atomistic system. As a result, we chose to modify the original PAINN architecture instead of CHIROPAINN.

Node input features The model employs a learnable atomic embedding function, $f_{\text{atom}} : \mathcal{A} \rightarrow \mathbb{R}^{d_f}$, to map atomic species to feature vectors, where d_f is the feature dimension. For continuous values, the embedding function $f_{\text{cont}} : \mathbb{R} \rightarrow \mathbb{R}^{d_f/2}$ is defined using a sinusoidal encoding:

$$[f_{\text{cont}}(x)]_i = \begin{cases} \sin(2\pi f_{\lfloor i/2 \rfloor} x) & i \text{ odd,} \\ \cos(2\pi f_{\lfloor i/2 \rfloor} x) & i \text{ even,} \end{cases} \quad (25)$$

where f_i ($i \in \llbracket 1, d_f/4 \rrbracket$) are frequencies sampled from a standard normal distribution $\mathcal{N}(0, 1^2)$ and fixed during training. The invariant node embedding for atom j is computed as $f_{\text{atom}}(a_j) + (f_{\text{cont}}(T/1000) \oplus f_{\text{cont}}(t))$, for temperature T and flow matching time t . Rather than initializing equivariant node features to zeros as in the original model, they are initialized from the current step displacement as $\mathbf{D}_t \otimes \mathbf{w} \in \mathbb{R}^{n \times 3 \times d_f}$, where $\mathbf{w} \in \mathbb{R}^{d_f}$ is a learnable weight vector.

Message passing For clarity and ease of comparison, we use the notation from the PAINN paper Schütt et al. (2021) for this part. As described in the main text, we leverage information from two sets of coordinates, \mathbf{X}_τ and $\mathbf{X}_\tau + \mathbf{D}_t$, during message passing. To simplify computation, we define the edges using a radius cutoff graph based on \mathbf{X}_τ , avoiding the need to reconstruct the neighbor graph at each flow matching step t . When expanding distances into radial basis functions, we shift the distance by 0.5 \AA . Unlike physically realistic atomistic systems, during flow integration,

the structure $\mathbf{X}_\tau + \mathbf{D}_t$ may experience atomic clashes. Since Bessel function values change most significantly at small radii, shifting the distances helps reduce variance in the edge features.

In the message functions that use continuous-filter convolutions, we apply elementwise addition of the filters corresponding to the two distances, $\|\vec{r}_{ij,1}\|$ and $\|\vec{r}_{ij,2}\|$. To avoid introducing unintended permutation symmetry between two geometries, we use two distinct filters ($\mathcal{W}'_{v_s,k}$ in Eq. (27b)) for the respective unit vector directions. The invariant message update Eq. (26a) (Eq. (7) in the original paper) is modified as Eq. (26b):

$$\Delta \mathbf{s}_i^m = \sum_j \phi_s(\mathbf{s}_j) \circ \mathcal{W}_s(\|\vec{r}_{ij}\|), \quad (26a)$$

$$\Delta \mathbf{s}_i^m = \sum_j \phi_s(\mathbf{s}_j) \circ [\mathcal{W}_s(\|\vec{r}_{ij,1}\|) + \mathcal{W}_s(\|\vec{r}_{ij,2}\|)], \quad (26b)$$

and the equivariant message update Eq. (27a) (Eq. (8) in the original paper) is modified as Eq. (27b):

$$\Delta \vec{v}_i^m = \sum_j \vec{v}_j \circ \phi_{vv}(\mathbf{s}_j) \circ \mathcal{W}_{vv}(\|\vec{r}_{ij}\|) + \sum_j \phi_{vs}(\mathbf{s}_j) \circ \mathcal{W}'_{v_s}(\|\vec{r}_{ij}\|) \frac{\vec{r}_{ij}}{\|\vec{r}_{ij}\|}, \quad (27a)$$

$$\begin{aligned} \Delta \vec{v}_i^m = & \sum_j \vec{v}_j \circ \phi_{vv}(\mathbf{s}_j) \circ [\mathcal{W}_{vv}(\|\vec{r}_{ij,1}\|) + \mathcal{W}_{vv}(\|\vec{r}_{ij,2}\|)] \\ & + \sum_{k \in \{1,2\}} \sum_j \phi_{v_s,k}(\mathbf{s}_j) \circ [\mathcal{W}'_{v_s,k}(\|\vec{r}_{ij,1}\|) + \mathcal{W}'_{v_s,k}(\|\vec{r}_{ij,2}\|)] \frac{\vec{r}_{ij,k}}{\|\vec{r}_{ij,k}\|}. \end{aligned} \quad (27b)$$

Table A1: **Effect of PAINN modification.** Evaluation metrics for the *Propagator* model using a uniform scale ($\sigma = 1$) Maxwell-Boltzmann prior distribution. Standard deviations are from three independent generations.

Train T (K)	Inference T (K)	Model	$\log \text{MSD}_{\text{Li}}$ MAE (\downarrow)	$\log \text{MSD}_{\text{Li}}$ ρ (\uparrow)	$\log \text{MSD}_{\text{frame}}$ MAE (\downarrow)	Stable traj. % (\uparrow)
800	800	PAINN	0.976 ± 0.008	0.344 ± 0.005	1.217 ± 0.009	38.1 ± 1.3
		Modified PAINN	0.396 ± 0.006	0.779 ± 0.009	0.274 ± 0.003	99.4 ± 0.1

Performance comparison Since we use \mathbf{D}_t to initialize the vector node features, the additional positional input $\mathbf{X}_\tau + \mathbf{D}_t$ could be omitted without losing information, allowing the use of the original PAINN model. Table A1 presents a comparison of the metrics from Table 1 between the original and modified PAINN models. The results show a significant difference between the two models, highlighting the importance of incorporating the intermediate structure $\mathbf{X}_\tau + \mathbf{D}_t$.

D.3 TRAINING ALGORITHMS

The training algorithms for the *Propagator* and *Corrector* are shown in Algorithms A1 and A2, respectively. When training on the universal dataset, material compositions are sampled uniformly by assigning a sampling weight inversely proportional to the number of materials in the training set with that specific composition.

D.4 TRAINING AND INFERENCE HYPERPARAMETERS

The training and model hyperparameters are summarized in Table A2. Additionally, validation loss was evaluated every 1,250 training steps, with early stopping triggered if the validation loss did not improve after ten evaluations. The model parameters corresponding to the lowest validation loss were used for inference.

For *Propagator* in the AIMD dataset, we replaced the prior classifier with fixed prior scale parameters for each temperature, determined based on the MSD values from the training trajectories. Additionally, in both LGPS and LPS, the frame atoms did not exhibit diffusive behavior, so we applied a uniform prior scale for these atoms. The prior scales used were $(\sigma_{\text{Li}}^{\text{small}}, \sigma_{\text{Li}}^{\text{large}}) = (1, 10)$ for

Algorithm A1: LiFLOW Propagator Training**Input:** Dataset of time-separated material structures \mathcal{D} **Output:** Optimized *Propagator* parameter θ **while Training do**

```

Sample data  $(\mathbf{X}_\tau, \mathbf{X}_{\tau+\Delta\tau}, \mathbf{L}, \mathbf{a}, T) \sim \mathcal{D}$ 
Sample flow time  $t \sim \mathcal{U}(t; 0, 1)$ 
Sample Propagator prior  $\mathbf{D}_0 \sim \mathcal{N}(\mathbf{D}_0; \mathbf{0}, \text{diag}(\boldsymbol{\sigma})^2 \otimes \mathbf{I}_3)$ 
 $\mathbf{D}_1 \leftarrow \mathbf{X}_{\tau+\Delta\tau}$  // True displacements
 $\mathbf{D}_t \leftarrow (1-t)\mathbf{D}_0 + t\mathbf{D}_1$  // Interpolated displacements (Eq. (11))
 $u_t(\mathbf{D}_t|\mathbf{D}_1) \leftarrow (\mathbf{D}_1 - \mathbf{D}_t)/(1-t)$  // Conditional flow (Eq. (11))
 $v_t(\mathbf{D}_t; \theta) \leftarrow \text{Propagator}(\mathbf{D}_t, \mathbf{X}_\tau, \mathbf{L}, \mathbf{a}, T, t; \theta)$ 
 $\mathcal{L}_{\text{CFM}}(\theta) \leftarrow \|v_t(\mathbf{D}_t; \theta) - u_t(\mathbf{D}_t|\mathbf{D}_1)\|^2$  // CFM regression objective (Eq. (2))
 $\theta \leftarrow \text{Update}(\theta, \nabla_\theta \mathcal{L}_{\text{CFM}}(\theta))$  // Parameter update

```

Algorithm A2: LiFLOW Corrector Training**Input:** Dataset of time-separated material structures \mathcal{D} **Output:** Optimized *Corrector* parameter θ **while Training do**

```

Sample data  $(\cdot, \mathbf{X}_\tau, \mathbf{L}, \mathbf{a}, T) \sim \mathcal{D}$ 
Sample flow time  $t \sim \mathcal{U}(t; 0, 1)$ 
Sample Corrector prior  $\mathbf{D}_0 \sim \mathcal{N}(\mathbf{D}_0; \mathbf{0}, \text{diag}(\boldsymbol{\sigma})^2 \otimes \mathbf{I}_3)$ 
Sample noise scale  $\boldsymbol{\sigma}' \sim \mathcal{U}(\boldsymbol{\sigma}'; \mathbf{0}, \sigma_{\max} \mathbf{1}_n)$ 
Sample positional noise displacement  $\mathbf{D}|\boldsymbol{\sigma}' \sim \mathcal{N}(\mathbf{D}; \mathbf{0}, \text{diag}(\boldsymbol{\sigma}')^2 \otimes \mathbf{I}_3)$ 
 $\tilde{\mathbf{X}}_\tau \leftarrow \mathbf{X}_\tau + \mathbf{D}$  // Noisy positions
 $\mathbf{D}_1 \leftarrow -\mathbf{D}$  // True denoising displacements
 $\mathbf{D}_t \leftarrow (1-t)\mathbf{D}_0 + t\mathbf{D}_1$  // Interpolated displacements (Eq. (11))
 $u_t(\mathbf{D}_t|\mathbf{D}_1) \leftarrow (\mathbf{D}_1 - \mathbf{D}_t)/(1-t)$  // Conditional flow (Eq. (11))
 $v_t(\mathbf{D}_t; \theta) \leftarrow \text{Corrector}(\mathbf{D}_t, \tilde{\mathbf{X}}_\tau, \mathbf{L}, \mathbf{a}, T, t; \theta)$ 
 $\mathcal{L}_{\text{CFM}}(\theta) \leftarrow \|v_t(\mathbf{D}_t; \theta) - u_t(\mathbf{D}_t|\mathbf{D}_1)\|^2$  // CFM regression objective (Eq. (2))
 $\theta \leftarrow \text{Update}(\theta, \nabla_\theta \mathcal{L}_{\text{CFM}}(\theta))$  // Parameter update

```

lithium atoms, and $\sigma_{\text{frame}} = 10^{-1/2}$ for LGPS and 1 for LPS. For the *Corrector*, we set the maximum noise scale to $\sigma_{\max} = 0.1$ for the $2 \times 2 \times 1$ supercell of LGPS and for all LPS experiments. For the larger $4 \times 4 \times 4$ supercell inference in LGPS, we used a *Corrector* trained with $\sigma_{\max} = 0.2$ to improve trajectory stability.

Table A2: Hyperparameters for training the *Propagator* and *Corrector* models.

Parameter	Value
Feature dimension	64
Radial basis functions	20
Message passing layers	3
Cutoff distance	5.0
Offset distance	0.5
Optimizer	Adam (Kingma & Ba, 2014)
Learning rate	0.0003
Gradient clipping norm	10.0
Batch size	16
Maximum training steps	125,000

We performed LiFLOW inference for $N_{\text{step}} = 150$ steps in the $2 \times 2 \times 1$ LGPS simulations and $N_{\text{step}} = 1000$ steps in the $4 \times 4 \times 4$ LGPS simulations, with a time step of $\Delta\tau = 1.005$ ps.

This corresponds to total simulation times of 150.75 ps and 1.005 ns, respectively. For the LPS simulations, we used $N_{\text{step}} = 250$ steps with a time step of $\Delta\tau = 1$ ps, resulting in a total simulation time of 250 ps. We used Euler integration with $N_{\text{flow}} = 10$ steps for all experiments.

D.5 IMPLEMENTATION DETAILS AND COMPUTATIONAL COST

We implemented the LiFLOW model using PyTorch (Paszke et al., 2019) and PyG (Fey & Lenssen, 2019) libraries. For MLIP-based simulations, we utilized MACE-MP-0 (mace-torch package, Batatia et al. (2024)) in combination with ASE (Larsen et al., 2017). Bayesian analysis of diffusivity and activation energy was performed using the kinisi package (McCluskey et al., 2024b). Training and inference of LiFLOW models were performed using a single NVIDIA RTX A5000 GPU. The training process for the Propagator and Corrector models, using early stopping, typically lasts between 45,000 and 70,000 steps. This corresponds to approximately 40–60 minutes of training, extending to up to two hours if the maximum step budget is reached. For AIMD simulation in Table 4, we used the Γ -point only version of VASP (vasp.gam, Hafner (2008)) with 48 cores of an Intel Xeon Gold 8260 CPU. The same input files used in the LGPS AIMD simulations were utilized for the benchmark.

E ADDITIONAL RESULTS

E.1 ISOTROPIC VS. MAXWELL–BOLTZMANN PRIOR

Table A3: **Effect of prior design.** Comparison between the isotropic prior and the scaled Maxwell–Boltzmann prior using different scale multipliers. Only the propagator model was used, and was trained and tested on 800 K trajectories.

Prior	Scale multiplier (σ)	log MSD _{Li} MAE (\downarrow)	log MSD _{Li} ρ (\uparrow)	log MSD _{frame} MAE (\downarrow)	Stable traj. % (\uparrow)
Isotropic	10^{-2}	0.726 ± 0.012	0.550 ± 0.008	0.900 ± 0.007	99.9 ± 0.1
	$10^{-1.5}$	0.498 ± 0.003	0.753 ± 0.008	0.318 ± 0.008	98.6 ± 0.2
	10^{-1}	0.531 ± 0.008	0.713 ± 0.008	0.454 ± 0.012	95.9 ± 0.2
	$10^{-0.5}$	0.551 ± 0.009	0.723 ± 0.004	0.470 ± 0.001	100.0 ± 0.0
	10^0	0.626 ± 0.005	0.712 ± 0.004	0.408 ± 0.002	100.0 ± 0.0
Maxwell–Boltzmann	10^{-1}	0.694 ± 0.002	0.563 ± 0.007	0.653 ± 0.003	88.1 ± 1.5
	$10^{-0.5}$	0.511 ± 0.004	0.682 ± 0.006	0.419 ± 0.004	99.8 ± 0.2
	10^0	0.396 ± 0.006	0.779 ± 0.009	0.274 ± 0.003	99.4 ± 0.1
	$10^{0.5}$	0.654 ± 0.002	0.694 ± 0.006	0.447 ± 0.005	99.4 ± 0.1
	10^1	0.577 ± 0.007	0.709 ± 0.009	0.339 ± 0.007	99.9 ± 0.1

E.2 UNIVERSAL MODEL

Examples of LiFLOW model inference trajectories for the universal model are presented in Fig. A4 (Page 24).

E.3 LGPS AIMD MODEL

The temperature extrapolation results, which extend from Fig. 3, are displayed in Fig. A3. The lithium diffusion trace for the LGPS simulations is provided in Fig. A5, and the 2-D negative log densities of lithium atoms are illustrated in Fig. A6 (Page 25).

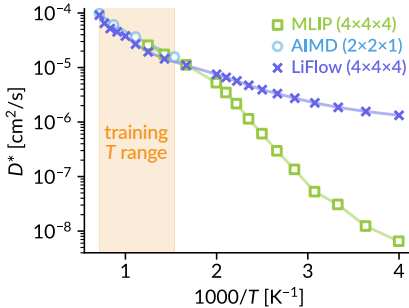


Figure A3: **Temperature extrapolation.** Lithium D^* is plotted as a function of $1000/T$ for LGPS ($\text{Li}_{10}\text{GeP}_2\text{S}_{12}$), extending the data from Fig. 3 (right) to lower temperatures (higher $1000/T$).

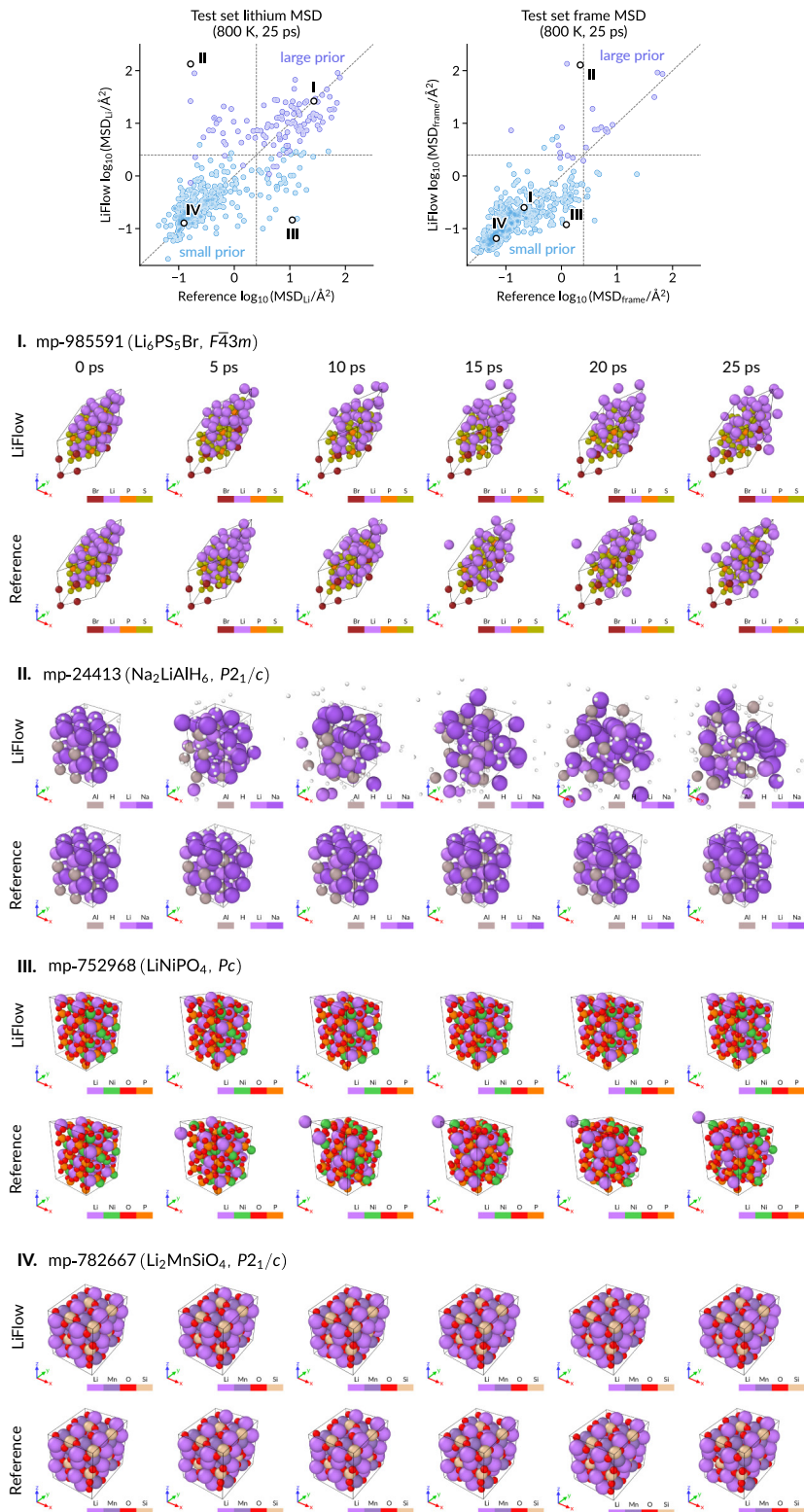


Figure A4: **Universal model inference example.** (Top) Parity plots comparing the log MSD values for lithium and frame atoms in 800 K simulations (reference vs. 25-step LiFlow inference) across 419 test materials. Data points are colored by their respective prior scales, with four annotated examples (I–IV) highlighted below. Dotted lines indicate the classification boundary between large and small priors. (Bottom) Reference and generated trajectories for the four annotated test set materials.

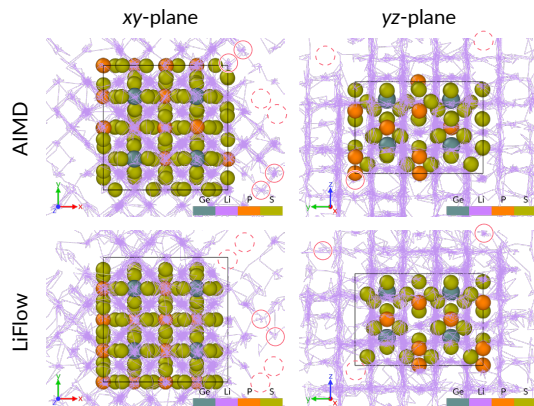


Figure A5: **Diffusion trace of lithium in LGPS simulations.** The diffusion traces of lithium atoms for 150 ps trajectories using LiFlow and AIMD at 900 K. Different lithium sites are accessed in different simulations, as indicated by circles: solid circles represent sites visited in the current simulation, while dotted circles indicate sites not visited in this simulation but visited in another.

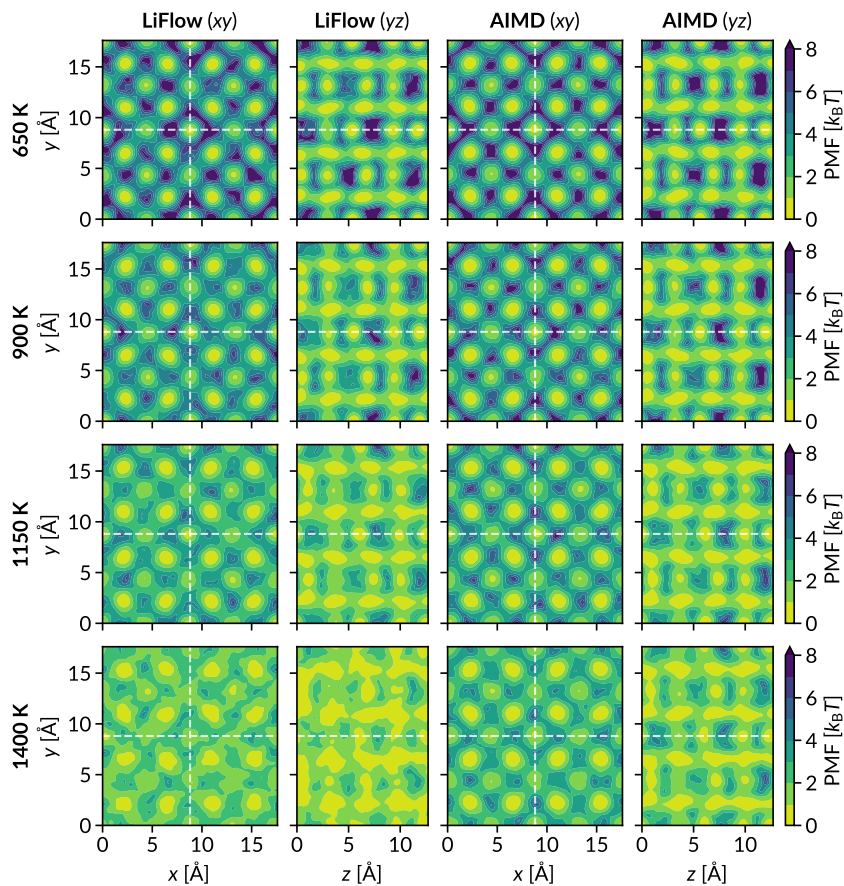


Figure A6: **Negative log densities for lithium in LGPS simulations.** The negative log density $-\log p(\mathbf{x})$, or potential of mean force (PMF) in units of $k_B T$, of lithium atoms in wrapped coordinates is shown for 150 ps trajectories using LiFlow and AIMD across different temperatures. For each method, the first and second columns correspond to projections along x - y and y - z planes, respectively. Dotted lines indicate the supercell boundaries.